5-2014

DIGITAL IMAGE PROCESSING FOR ULTRASONIC THERAPY AND TENDINOUS INJURY

Jacob Hammers
Clemson University, jacob.hammers@gmail.com

DIGITAL IMAGE PROCESSING FOR ULTRASONIC THERAPY AND TENDINOUS INJURY

A Thesis
Presented to
the Graduate School of
Clemson University

In Partial Fulfillment
of the Requirements for the Degree
Master of Science
Bioengineering

By
Jacob Elliott Hammers
May 2014

Accepted by:
Dr. Delphine Dean, Committee Chair
Dr. Brian Dean
Dr. David Kwartowitz

ABSTRACT

In this master's thesis, several digital image processing techniques are explored for potential in evaluation of Brightness mode (B-mode) ultrasound images. Currently, many processing techniques are utilized during ultrasound visualization in cardiovascular applications, mammography, and three-dimensional ultrasound systems. However, approaches that serve to aid the clinician in diagnostic assessment of tendinous and ligamentous injuries are more limited. Consequently, the methods employed below are aimed at reducing the dependence on clinician judgment alone to assess the healing stage and mechanical properties of tendinous injuries.

Initial focus concentrated on the use of entropy in texture analysis to relate a tendon's appearance in an ultrasound image to its mechanical integrity. Confounding effects such as motion artifacts and region of interest selection by the user limited the applicability of small regions selected for analysis, but general trends were observed when the entire visualized tendon or superficial background region was selected. Entropy calculations suggested a significant change in texture pattern for tendinous regions compared to the selected background regions.

In order to reduce the impact of motion artifacts and dependence of the texture analysis on manual identification of regions of interest, a Matlab® script was developed intended to isolate the tendinous regions of interest for further analysis. Methods for segmentation employed relied on a moving window Fourier Transform to compare local parameters in the image to a predefined window of tendinous tissue. Further assessment

of each local region benefited from parameterization of the local window's properties that focused on capturing indicators of mean pixel intensity, local variation in pixel intensity, and local directionality consistency derived from the spatial frequency patterns observed in the Fourier Transforms *via* comparison by the circular Earth Mover's Distance.

Results of the segmentation algorithm developed indicated the presence of directional consistency within the tendinous regions, and changes in the speckle pattern were observed for the image derived from mean intensity and local pixel intensity variation. However, non-tendinous regions were also identified for their directional consistency, limiting the applicability of the current process in tendinous region isolation. The results obtained for calculations of the circular Earth Mover's Distance improved slightly with the inclusion of temporal averaging and image registration, but still require improvement before implementation in clinical applications can be realized.

DEDICATION

This thesis is dedicated to my mother, Lori, the most determined person I have ever met, to my grandfather, father, sister, and girlfriend, all of whom never let me lose track of what is important in life. This thesis belongs to my family, for I never would have had the ambition, curiosity, discipline, or support I needed to succeed without them.

ACKNOWLEDGEMENTS

I would like to thank my advisor, Dr. Delphine Dean, for offering me support and guidance when I needed it and gave me the opportunity to pursue my passion. I would also like to thank my committee members, Dr. Brian Dean and Dr. David Kwartowitz, for mentoring me and providing me with the tools I needed to perform. Finally, thank you to the Clemson Bioengineering Department for supporting and empowering me through five of the most exciting years of my life.

TABLE OF CONTENTS

Page

Table of Contents (Continued)

Page

LIST OF FIGURES

Figure Page

List of Figures (continued)

Figure Page

CHAPTER I

INTRODUCTION TO ULTRASONIC THERAPY

1.1 Introduction

Medical ultrasound is a modality that is commonly used in a wide variety of applications due to a number of benefits it offers: it is non-invasive, non-ionizing, inexpensive, and has excellent temporal resolution.[2] It relies on application of high-frequency acoustics to a volume of interest in pulses and measurement of the reflected sound waves to generate an image. This functional method produces a negative correlation between resolution of ultrasonic images and penetration depth, as attenuation of acoustic waves within tissues is greater for the high frequencies that provide superior resolution. While ultrasound is utilized extensively to visualize soft tissues in the body, the large, abrupt change in density at the interface of a bone and the surrounding soft tissue results in almost total reflectance of the sound waves, preventing visualization of tissues beyond the interface. Despite these limitations, ultrasound imaging is a useful modality for many applications, from cardiovascular visualization to fetal examination to diagnosis of soft tissue disease and injury.[2]

There are approximately 16 million soft tissue injuries, including tendon and ligaments, reported in the United States each year.[3] Risk factors influencing the likelihood of a patient in the United States to suffer a tendinous rupture include overuse and predisposing conditions such as kidney failure, rheumatoid arthritis, diabetes, gout, and use of steroids.[3,4] As a method for diagnosis of soft tissue injuries, brightness mode (B-mode) ultrasound offers an inexpensive and effective screening method clinicians use

to assess the severity and nature of the injury. Assessment of such injuries for tendons and ligaments relies extensively on a clinician's ability to derive information from these images in order to distinguish between those requiring surgical intervention and those that may heal properly from physical therapy alone.[1,3] The potential benefit of a process that establishes objective metrics for a tendon's healing stage, mechanical properties, and severity of injury continues to drive demand for development.

The following chapters will discuss the factors involved in tendinous injuries, image acquisition of tendons *via* ultrasound, and employed image processing techniques aimed at improving the diagnostic quality of B-mode ultrasound images. Chapter 2 relates to a tendon's composition and the factors that lead to injury. Chapter 3 considers the benefits of current digital image processing techniques that offer potential for the isolation and parameterization of regions of interest. Chapter 4 discusses ultrasound image acquisition and texture parameterization. Chapter 5 concerns the processing techniques used in the development of a segmentation algorithm functioning to identify regions of interest.

1.2 References

[1] V. Ciriello, S. Gudipati, T. Tosounidis, P. Soucacos, and P. Giannoudis, "Clinical outcomes after repair of quadriceps tendon rupture: A systematic review," *Injury-International Journal of the Care of the Injured*, vol. 43, pp. 1931-1938, NOV 2012.

[2] G. Dougherty, *Digital Image Processing for Medical Applications*. California State University: Cambridge University, 2009.

[3] R. James, G. Kesturu, G. Balian, and B. Chhabra, "Tendon: Biology, Biomechanics, Repair, Growth Factors, and Evolving Treatment Options," *Journal of Hand Surgery*, vol. 33A, pp. 102-112, 2008.

[4] U. Longo, G. Garau, V. Denaro, and N. Maffulli, "Surgical management of tendinopathy of biceps femoris tendon in athletes," *Disability and Rehabilitation*, vol. 30, pp. 1602-1607, 2008.

CHAPTER II

TENDON FUNCTIONAL ANATOMY AND INJURIES

As the mechanical junction that permits locomotion, tendons and ligaments represent a critical load-bearing component of the musculoskeletal system. Due to the inherent difficulty in assessing the severity of tendinous injuries, the stage of healing of a tendon after injury, and predicting the mechanical properties of tendons, there is a great need for an improved understanding of the factors that affect tendinous injuries.[3,5,6,8,11,14] Critical elements of diagnostic process improvement in ultrasound imaging for the assessment of tendinous injuries are tendon composition, the natural mechanical behavior of tendon, its stages of healing and how injury impacts its mechanical integrity, current treatment methods and how they affect the healing process.

2.1 Tendon Composition

Tendons are rode-like bundles of cells and connective tissue. The cellular part of a tendon consists of tenoblasts, tenocytes, and chondrocytes. The tenoblasts and tenocytes cells are approximately 90% of this part of the tendon, while chondrocytes and other cells are the remaining 10%.[14] Tenocytes, mature tenoblasts, have a very low metabolic rate, which gives the cell high endurance while under large stresses. The mature nature of these cells also contributes to a slow healing process after injury.[14] Tenocytes synthesize type I collagen, which is the basic structural unit of the tendon. Type III collagen is also present, but in significantly smaller concentrations. Once the collagen is synthesized, it is excreted to the extracellular matrix where it is assembled into densely packed fibers

along the longitudinal axis of the tendon. Altogether, collagen accounts for approximately 75% of the dry weight of a tendon. Overall, the dry weight of a tendon is only 30% of the total mass. Another two percent is contributed to elastin.[8,14] Other components of the extracellular matrix include decorin, aggrecan, and biglycan that primarily serve as sites of attachment between collagen fibers.[8] The remaining 68% is water. Generally speaking, elastin fibers within the tendon contribute to the tendon's flexibility, whereas the collagen fibers within a tendon provide it with its considerable tensile strength.[12]

Morphologically, tendons are composed of a hierarchical structure in which many layers of bundles exist, as shown in Figure 2.1. Together with tenocytes, collagen fibrils bound together, forming collagen fibers, are the basic structural unit of tendons. Bundles of collagen fibers are bound together by a layer of connective tissue known as endotenon, forming fascicle functional units. Multiple fascicles and a sparse network of blood and lymphatic vessels are further bound together by a connective tissue layer known as the epitenon. Tendons are encapsulated in an areolar loose connective tissue layer, the paratenon, that allows blood vessels to permeate into deeper tendon tissue.[8,12,14] Other tendons that bend around a joint, such as those in the hand, are enclosed by a tendon sheath that is lubricated by the fluid produced from surrounding synovial cells, limiting sliding friction.[8] Vascularity in tendons is nonuniform; zones of compression, friction, and torsion have demonstrated hypovascularity. This relationship limits the blood flow of tendons at their insertions, which in turn reduces the rate of healing in these regions.[14]

The highly ordered and densely packed nature of tendons give them strength

equivalent to bone and are stronger per unit area than muscle.[8] A tendon with a cross sectional area of one square centimeter is capable of holding up to 1000 kg.[14] Furthermore, tendons are flexible and slightly extendable, allowing for a one to three percent elongation.[8] The body limits this ability of the tendon to extend in order to translate as much of the muscle force to the bone as possible. In spite of their strength, tendons do rupture and tear during some intense exercises or due to stress on the joint when it is in an unnatural position. The intensive exercise may cause a sudden over loading of force on the tendon, or over-extension of the tendon, leading to injury. It has been shown that patients with Achilles tendon ruptures see a high recurrence rate of two to eight percent.[6] These injuries often severely limit the patient's ability to use the joint due to risk of disrupting the healing process and causing re-injury.

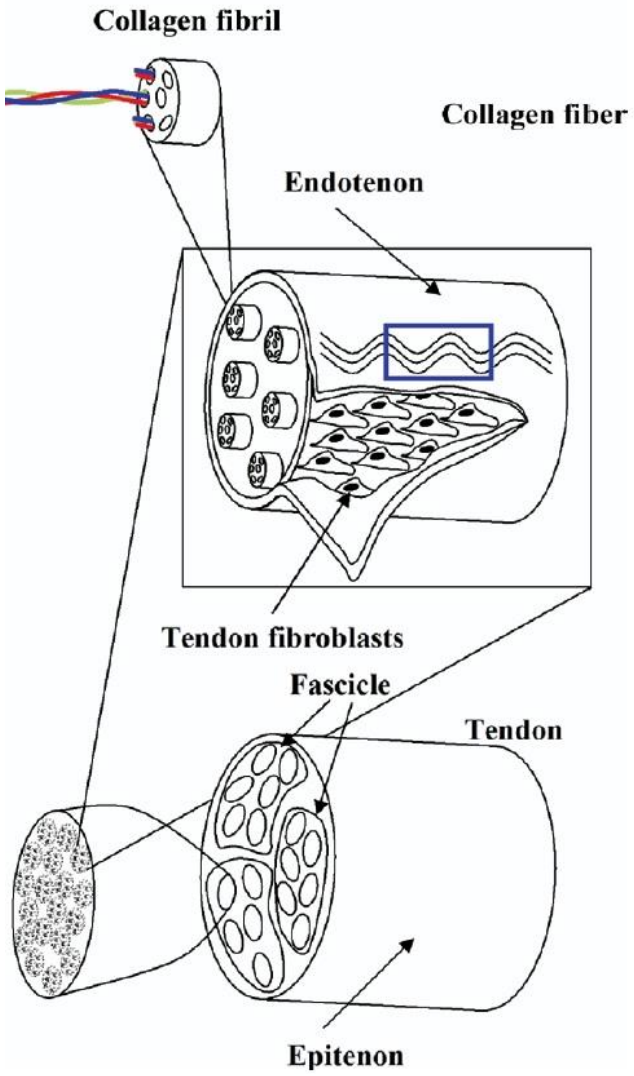

Figure 2.1: Diagram depicting hierarchical, bundled structure of tendon tissue. Note that the large number of parallel collagen fibers lends tendons impressive tensile strength, but make it more susceptible to shear forces. (Adapted from [8] James et al. 2008).

2.2 Mechanical Properties of Tendon

The mechanical properties of tendon follow directly from its structure. Their complex composition containing multiple fiber types and sizes and the numerous paradigms by which tendinous tissue extends and contracts yields a non-Newtonian mechanical behavior. As viscoelastic tissues, tendons display stress relaxation and creep

responses to mechanical loading.[14] Figure 2.2 summarizes the primary response of tendinous tissue to mechanical loading. Below two percent strain, the toe region of tendon elongation represents the region in which the collagen fibers, whose resting state is slightly crimped, flatten into linear arrangements. As the potential for such extension becomes exhausted around two percent strain, further elongation between two and four percent strain occurs as the fibrils composing each collagen triple helix slide past one another.[14] Failure of the crosslinks binding collagen fibers together occurs in the four to eight percent strain region as the fibers begin to slide past one another, resulting in microscopic damage to the stretched tendon.[12] If further stress is applied to the tendon, macroscopic failure of the tendon is a result of intrafibril molecular bond breakage as the applied energy overcomes the bond energy holding together the atoms within each collagen fibril.

A tendon's tensile strength is proportional to its cross-sectional thickness, with a square centimeter cross-sectional area corresponding to load-bearing capacity of approximately one kilogram.[14] The rate at which a load is applied to tendon affects the apparent strength of that tendon; physiologic loading during running measured in the Achilles tendon exceed 12.5 times body weight that is applied at comparatively low frequency.[10] Tension applied at a faster rate increases risk of tendon rupture at a given applied load.[1,10] In many cases, clinically reported tendon injuries have been found to be associated with degenerative changes within the tendon tissue, which is expected to cause a predisposition for tendinous injury. While there are many possible precursors to tendinous injury, multiple factors are commonly involved that result in tendon rupture.[14]

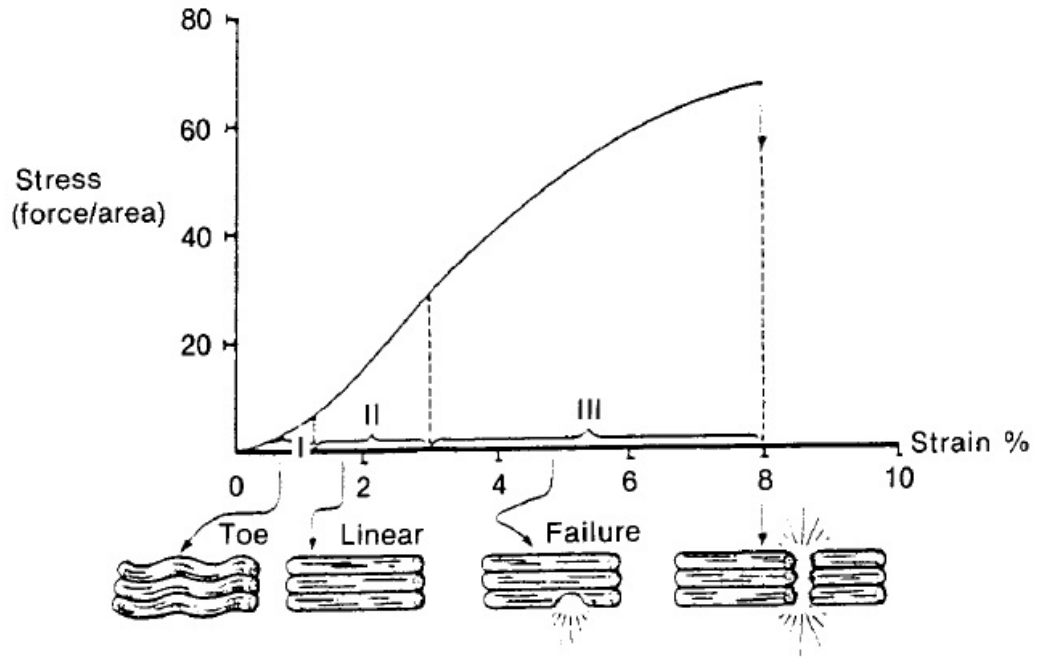

Figure 2.2: Stress-strain relationship of tendons separated by regional paradigm and mechanism of elongation. Forces exerted on tendons during normal use typically do not exceed magnitudes capable of causing more than a four percent strain. (Adapted from [12] O'Brien 1992).

2.3 Tendon Healing Process

Ruptured tendon tissue can be visualized using ultrasound due to a change in the speckle pattern of the tissue.[3,5] Tendon healing can be divided into three stages: the inflammatory response, the proliferative stage, and the remodeling stage. Each stage, while possessing unique characteristics, partially overlap with the adjacent stages.[14] During the initial inflammatory response to tendon injury, degradation of wound debris and necrotic material occurs by migration of monocytes and subsequent maturation of these cells into macrophages. During this phase, angiogenesis is stimulated that results in the elevated levels of vascularization evident in tendinous tissue even years after injury.[16] Tenocyte migration and deposition of type-III collagen at the site of injury is stimulated,

leading to a transition into the proliferative phase after a period of a few days.[14]

During the proliferative phase, tenocyte proliferation, activity, and recruitment of fibroblasts to the wound site is responsible for the deposition of proteoglycans, ground substance and tropocollagen.[8,14] Histological evaluation of post-injury tendon tissue has demonstrated increased cellularity due to the proliferation of fibroblasts accompanied with increased vascularity and deterioration of the fiber structure.[3,4,8,9,11,12,14,16] This change in histological composition of a tendon following injury into scar-like tissue is accompanied by a decrease in tensile strength and, consequently, increased risk of tendon rupture. Immobilization of a tendon for long periods of time results in a 20% to 40% loss of its ground substance.[12] A tendon that has healed from trauma becomes tendon-like in composition, but never fully regenerates, shown in Figure 2.3. By the conclusion of the proliferative stage, the resulting tissue contains substantially increased cellularity, vascularity, water content, and matrix components deposited by tenocytes and inflammatory cells.[8]

Six to ten weeks after injury, the remodeling stage begins. Over the course of several years, cellularity of the tendon slowly decreases, matrix synthesis slows, and type-I collagen, the form of organized linear collagen to which tendons owe their tensile strength, increases as deposition of type-III collagen slows.[8,14] The changes effected in the remodeling stage are evident over several years as the healing tissue increases in stiffness and the tensile strength improves, but histological evidence of the injury remains even up to six years post-injury, and the mechanical properties never fully recover.[16]

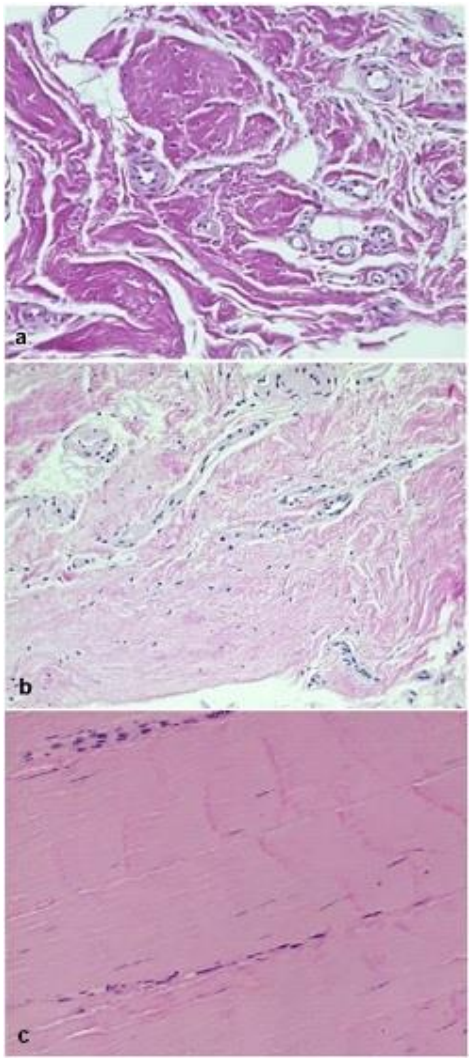

Figure 2.3: Histology of patellar tendon tissue that observes the stages of healing after harvesting of the central third for reconstruction surgery (approximate original magnification of 200x). Depicted in a) and b) is the healing stages of the patellar tendon in an 18 year old male undergoing anterior cruciate ligament reconstruction surgery two and size years after surgery, respectively. When compared with c), which shows the histology of 25 year old male's patellar tendon as a control specimen, it can be seen that injury to a tendon results in reduced fiber linearity, increased vascularity, and substantially increased cellularity present even through the long term remodeling stage of healing and tendon repair (Adapted from [16] Svensson et al. 2005)**.**

The mechanisms by which these changes in tissue activity and composition occur fall into two main categories; extrinsic healing responses involve invasion of the native tissue by inflammatory cells that initiate healing while cellular activity originating in the epitenon and endotenon layers leads to the intrinsic healing response.[8,14] Many factors

influence the extent to which each pathway occurs, including injury severity, location, and motion of the tendon.[3,4,8,11,14] Typically, extrinsic healing dominates in the proliferative phase yielding to increased intrinsic healing activity in the remodeling phase.[8] Figure 2.4 displays the responses to tendon trauma that dominate at each stage of injury.

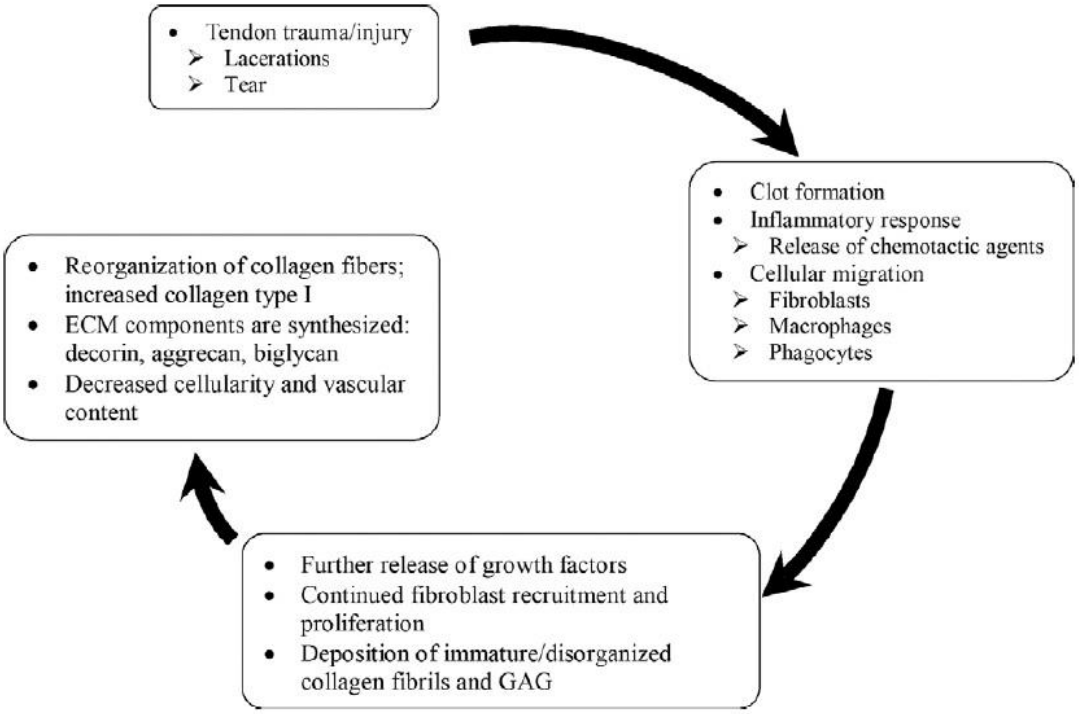

Figure 2.4: Stages of healing in tendinous injury, pictured in clockwise progression: tendon injury, inflammatory stage, proliferative stage, and remodeling stage. GAG=glycosaminoglycans, ECM=Extracellular Matrix (Adapted from [8] James et al 2008)**.**

Note that the matrix components responsible for interfibril collagen articulation and alignment (decorin, aggrecan, biglycan) are primarily synthesized in the remodeling stage. As a result, earlier healing stages have disorganized collagen fibers that do not present the linear alignment typical of healthy tendon tissue. The reduced availability of these complexes during the earlier healing stages results in a weakening of the tendon's

strength in its toe region where most physiological loading occurs. However, prolonged mobilization of an injured tendon has been shown to lead to reduce water and proteoglycan content while increasing tissue atropy.[8,14] Loading of the tendon during the inflammatory stage not only prevents the effects of immobilization, but also promotes improved collagen synthesis and fiber alignment.[14] This demonstrates the importance of careful monitoring of the healing stage of an injured tendon in order to take appropriately timed steps to promote the development of healthy tissue while limiting risk of further injury.

2.4 Tendon Treatment Options

Currently, there are many approaches that attempt to accelerate the rate and extent of healing of an injured tendon.[3,4,8,11,14,15] These solutions include extracorporeal shock wave therapy, applying direct current, laser therapy, and radiofrequency coblation. Some techniques incorporate gene therapy and tissue engineering into the treatment process to promote superior and more complete tendon healing.[5] Generally, modern physical treatment balances immobilization and stimulation of the tendon during healing due to its poor mechanical properties after rupture and the increased risk of further injury.[8] Physical therapy in this paradigm relies on intermittent, precisely timed mechanical stimulation.[3]

Other treatment options rely on effecting an change in the expression of growth factors and the biochemical response that accompanies tendinous healing, the basis for extracorporeal shock wave therapy.[2,7,14] While such treatments were successful in study conducted using a rat model, a double blind, randomized trial for humans demonstrated

that the treatment showed little effect over a sham treatment offered to the control group in noncalcific rotator cuff injuries.[2,14,15] In another trial, calcific rotator cuff injuries responded positively to extracorporeal shock wave therapy proportional to the total energy delivered.[7] The proposed mechanism of action of this therapy involves the stimulation of angiogenesis and increased expression of vascular endothelial growth factor (VEGF), transforming growth factor-β1 (TGF-β1), and insulin-like growth factor 1 (IGF-1), all of which mediate aspects of the healing process. Care must be exercised when employing this treatment method, however, which has been demonstrated to cause necrosis, fibrosis, and inflammation in rabbit tendons.[13,14]

Stem cell and tissue engineering approaches are also being explored as potential treatment options to bridge the gap between injury and functional recovery of the tendon. For injuries in which a tendon has lost its capacity to withstand the loads associated with transferring action of a muscle to a bone, the tissue engineering approach proposes to implant a scaffold material and mesenchymal stem cells to encourage colonization of the scaffold, thereby restoring mechanical integrity.[14] However, the specific parameters promoting the most preferred outcome with this approach, such as scaffold material, cell culture, and seeding density, have not yet been established.

An emerging therapy option known as radiofrequency coblation the generation of reactive plasma to degrade soft tissues, which was shown to stimulate angiogenesis in rabbits and may relieve pain in tendinous injuries.[14] Before concrete conclusions may be drawn about the benefit of this therapy, broader human trials are required for validation. Another experimental approach proposes to improve the healing outcome by direct

application of TGF-β1, IGF-1, and cytokines to the wounded tissue, but has yet to be studied extensively.[8]

In conclusion, while integration of the many promising new treatment approaches remains a critical objective for improving functional healing of tendons, surgery or physical therapy remain the options with greatest success in the clinic today.[3,8] Except in the most severe cases, surgery is usually considered once physical therapy alone has not proven successful.[3] A variety of surgical techniques are employed that are selected from after considering tendon location, injury severity, and surgeon preference. In most cases, the paratenon is stripped away and the ruptured tissue is removed.[3] With current standard technologies, tendon injury management continues to challenge society. As demonstrated, if physical therapy is too aggressive, risk of reinjury becomes a major concern. However, physical therapy that fails to adequately stimulate the tendon during healing could result in a poor outcome due to atrophy and excess generation of scar-like tissue.[3,8] For these reasons, there is a great need for methods that improve the diagnostic quality of screening tools, namely ultrasonography, in assessing the healing stage and mechanical properties of an imaged tendon. In order to assist clinicians in the development of an appropriate physical therapy regimen for each patient, an objective, automated parameterization of the tendinous region of interest in the ultrasound image is preferred. It is therefore appropriate to develop image processing techniques that isolate tendinous regions from B-mode ultrasound images as well as distinguish between the texture patterns of tendons at different stages of healing in order to correlate such parameters to the predicted mechanical properties of each tendon.

2.5 References

[1] D. L. Butler, E. S. Grood, F. R. Noyes, and R. F. Zernicke, "Biomechanics of ligaments and tendons," *Exerc Sport Sci Rev*, vol. 6, pp. 125-81, 1978.

[2] Y. J. Chen, C. J. Wang, K. D. Yang, Y. R. Kuo, H. C. Huang, Y. T. Huang, *et al.*, "Extracorporeal shock waves promote healing of collagenase-induced Achilles tendinitis and increase TGF-beta1 and IGF-I expression," *J Orthop Res*, vol. 22, pp. 854-61, Jul 2004.

[3] V. Ciriello, S. Gudipati, T. Tosounidis, P. Soucacos, and P. Giannoudis, "Clinical outcomes after repair of quadriceps tendon rupture: A systematic review," *Injury-International Journal of the Care of the Injured*, vol. 43, pp. 1931-1938, NOV 2012.

[4] R. Clayton and C. Court-Brown, "The epidemiology of musculoskeletal tendinous and ligamentous injuries," *Injury-International Journal of the Care of the Injured*, vol. 39, pp. 1338-1344, DEC 2008.

[5] G. Dougherty, *Digital Image Processing for Medical Applications*. California State University: Cambridge University, 2009.

[6] D. García-Germán, R. Rubio-Quevedo, J. Lopez-Goenaga, and J. Martin-Guinea, "Achilles tendon recurrent rupture following surgical repair: report on two cases," *Foot Ankle Surg*, vol. 15, pp. 152-4, 2009.

[7] L. Gerdesmeyer, S. Wagenpfeil, M. Haake, M. Maier, M. Loew, K. Wörtler, *et al.*, "Extracorporeal shock wave therapy for the treatment of chronic calcifying tendonitis of the rotator cuff: a randomized controlled trial," *JAMA*, vol. 290, pp. 2573-80, Nov 2003.

[8] R. James, G. Kesturu, G. Balian, and B. Chhabra, "Tendon: Biology, Biomechanics, Repair, Growth Factors, and Evolving Treatment Options," *Journal of Hand Surgery*, vol. 33A, pp. 102-112, 2008.

[9] J. Kartus, T. Movin, N. Papadogiannakis, L. Christensen, S. Lindahl, and J. Karlsson, "A radiographic and histologic evaluation of the patellar tendon after harvesting its central third," *American Journal of Sports Medicine*, vol. 28, pp. 218-226, MAR-APR 2000.

[10] P. V. Komi, S. Fukashiro, and M. Järvinen, "Biomechanical loading of Achilles tendon during normal locomotion," *Clin Sports Med*, vol. 11, pp. 521-31, Jul 1992.

[11] U. Longo, G. Garau, V. Denaro, and N. Maffulli, "Surgical management of tendinopathy of biceps femoris tendon in athletes," *Disability and Rehabilitation,* vol. 30, pp. 1602-1607, 2008.

[12] M. Obrien, "Functional Anatomy and Physiology of Tendons," *Clinics in Sports Medicine,* vol. 11, pp. 505-520, JUL 1992.

[13] J. D. Rompe, C. J. Kirkpatrick, K. Küllmer, M. Schwitalle, and O. Krischek, "Dose-related effects of shock waves on rabbit tendo Achillis. A sonographic and histological study," *J Bone Joint Surg Br,* vol. 80, pp. 546-52, May 1998.

[14] P. Sharma and N. Maffulli, "Current concepts review tendon injury and tendinopathy: Healing and repair," *Journal of Bone and Joint Surgery-American Volume,* vol. 87A, pp. 187-202, JAN 2005.

[15] C. A. Speed, C. Richards, D. Nichols, S. Burnet, J. T. Wies, H. Humphreys, *et al.*, "Extracorporeal shock-wave therapy for tendonitis of the rotator cuff. A double-blind, randomised, controlled trial," *J Bone Joint Surg Br,* vol. 84, pp. 509-12, May 2002.

[16] M. Svensson, J. Kartus, L. Christensen, T. Movin, N. Papadogiannakis, and J. Karlsson, "A long-term serial histological evaluation of the patellar tendon in humans after harvesting its central third," *Knee Surgery Sports Traumatology Arthroscopy,* vol. 13, pp. 398-404, JUL 2005.

CHAPTER III:

DIGITAL IMAGE PROCESSING TECHNIQUES

Digital image processing is a field of signal processing that has found applications in almost every medical image modality, as well as innumerable applications in the computer-based society in which we live.[13] It is a concept that refers to the process by which a sampled signal from a sensor array is quantized, after which one or more mathematical operations is applied to transform the image to the displayed image. The general goal of such operations is to improve the image quality by some metric of image enhancement. Such metrics include, but are not limited to, signal-to-noise ratio (SNR), image sharpness, image contrast, or frequency domain exclusion. The processes applied fall into five main categories: image enhancement, image restoration, image analysis, image compression, and image synthesis. The application of image processing discussed in Chapter One relates to image analysis, a process that involves the parameterization of features within an image for the purpose of regional isolation, known as image segmentation, or pattern recognition.[3] Sophisticated segmentation algorithms are responsible for the facial identification procedure in many camera as well as gesture recognition in the Xbox Kinect™ system.[14]

Image analysis is particularly useful for texture identification.[3,5,8,12,18] The first example of this, published in 1991 by Dong-Chen He and Li Wang, established the foundation for parameterization that would allow for automated classification of surface textures pictured in an image.[5] He and Wang defined a number of parameters useful for such classifications, each providing specific metrics about the properties of the input

image. The features defined include black-white symmetry, geometric symmetry, degree of direction, and orientation specific features: micro-horizontal structure defined in each direction, and central symmetry. Three of these features were used to parameterize twelve sample texture images of such things as beach sand, water, and pressed cork. The process depicted in this work laid the groundwork for many modern texture discrimination algorithms in use today.

3.1 Spatial Dependency and Texture Analysis in Image Processing

He and Wang's parameters were all derived from the spatial domain of the image; that is, the functional texture unit from which each of the parameters was calculated is represented as a pixel and all its neighbors, forming a three by three local neighborhood in which each parameter could be defined. Therefore, the defined procedure belongs to a category of algorithms that retain spatial information within the output value. Other metrics of an image do not retain spatial information; one of the most common examples of a spatially independent image processing algorithms is the histogram. An image's histogram loses all dependency on individual pixel location during the summation of each brightness value a pixel can be assigned. Regardless of location in the image, two pixels of the same brightness in an image are identical when the histogram is computed. The normalized histogram of an image, the probability density function (PDF), is commonly used in image processing as an analytical device for evaluating an image's contrast, dynamic range, and overall brightness. Mathematical functions applied to the PDF can be used to alter an image's appearance in techniques known as histogram normalization and

histogram equalization.[3] These transformations are often utilized as image enhancement algorithms in an attempt to improve an image's quality.

In many applications, output that is dependent on the spatial information in an image is desired. Such dependence is the basis of texture analysis for images. One method used to assess an image's texture is through application of information theory and calculation of a region's entropy. In order to compute a region's entropy, one must first understand that the information content of a pixel, as a measure of its reduction of uncertainty, is given by Equation 3.1. That is, a common pixel value in a region of interest contains little information, and subsequently has a low entropy value.

$$I(E) = \log\left(\frac{1}{P(E)}\right) = -\log P(E)$$

Equation 3.1: Calculation of a unit's information content, where I(E) is the unit's information content, and P(E) is the probability each unit has of carrying that same information (i.e. pixels of the same value) (Adapted from [3] *Digital Image Processing for Medical Applications*)**.**

For binary outputs, the base of the logarithms shown in Equation 3.1 becomes two, and the unit of information being computed is the bit, for two events that may occur with equal probability. For situations in which the probability of each output is not equal, as in images containing features other than random noise, Equation 3.2 offers a first-order estimate of the entropy in a region of interest.

$$H = -\sum_{i=0}^{2^n-1} P(a_i)I(a_i) = -\sum_{i=0}^{2^n-1} P(a_i)\log_2 P(a_i)$$

Equation 3.2: Equation for the first order approximation of entropy (H) for a region of interest, in bits per pixel, where $P(a_i)$ = the probability of occurrence of that information state, $I(a_i)$ = the information content of that state, n = the number of bits that are needed to define the number of unique states in the image possible value range: 2^n. The summation is evaluated over 2^n-1 to compensate for the possibility of a zero value (Adapted from [3] *Digital Image Processing for Medical Applications*)**.**

Evaluating this equation, it can be seen that an image consisting of a number of pixels, all with the same value, has an entropy of zero, whereas an image in which all possible values occur with equal probability has the maximum possible entropy defined for an image of that size and bit-depth. Note that this first order evaluation of entropy still fails to retain any spatial information; the summation in Equation 3.2 is independent of pixel location. Entropy does provide an indication of a region's texture, however, by offering a measure of a region's local pixel variation in intensity. This has been utilized successfully in outcome prediction for pathological breast tissues.[3]

In order to retain spatial dependency of entropy calculations over a region of interest, it is necessary to derive entropy over domains other than the two-dimensional spatial domain. This is commonly accomplished by derivation of the gray-level co-occurrence matrix (GLCM). The GLCM is a matrix containing the number of instances in a region of interest in which one information state occupies a location relative to a specific direction from another.

For images, the GLCM tracks the number of instances in which a given pixel intensity occurs, in a given directional vector chosen by the user, relative to another. The direction selected indicates the alignment along which the GLCM retains spatial

information. Construction of a GLCM from a sample matrix is shown in Figure 3.1.

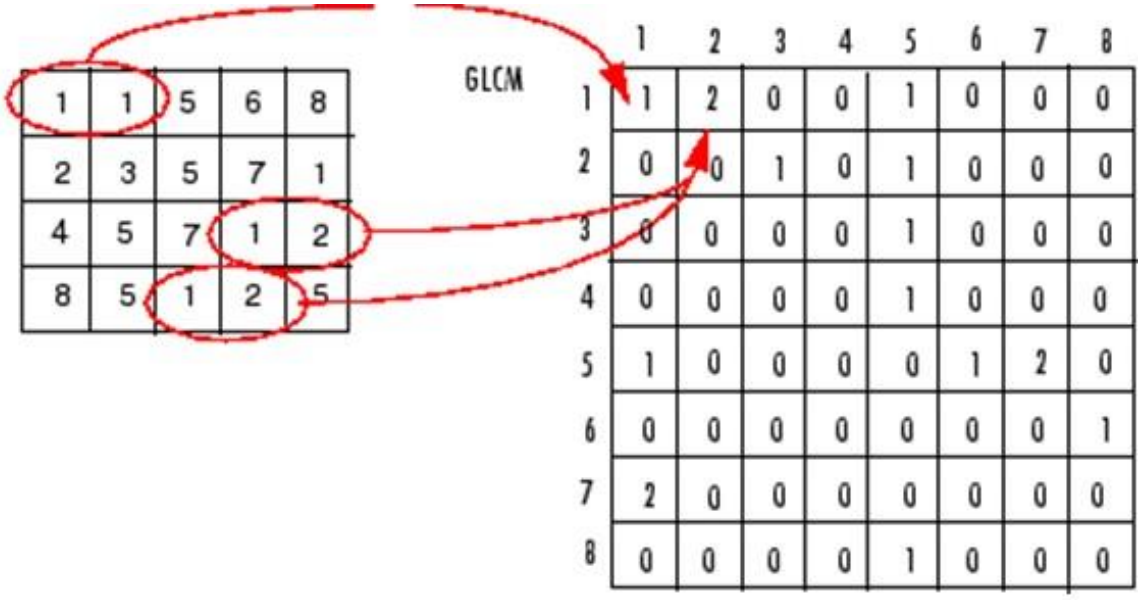

Figure 3.1: Depiction of the generation of a GLCM (right) from a sample matrix (left). The direction defined in this instance is a horizontal vector one pixel in magnitude; that is, the GLCM generated is for pixels in the sample matrix in which one occurs directly to the right of the other. A pixel with a value of one occurs adjacent to a pixel with a value of one exactly one time in the sample matrix. Therefore, the value stored in the GLCM at position (1,1) is one (Adapted from [4] *Digital Image Processing*)**.**

Note that summation of the GLCM along each row, generating a column vector, is the histogram of the original image. This indicates that the spatial information of a GLCM is retained only in one direction. Consequently, calculations derived from the GLCM also retain spatial information in that direction.[3,4]

3.2 Frequency Domain Image Processing and Analysis

A well-established process in image processing known as the Fourier transform involves the expression of a function or, in two dimensions, an image, as a summation of sinusoidal waves. This transform has been utilized in innumerable applications across

many of the categories in digital image processing, including image enhancement, image restoration, image analysis, and image reconstruction.[1,3,4,6,10,11,12,13,18] One benefit of the Fourier transform related to images that has contributed to its success is the ability to easily identify and filter out anomalies in the frequency domain whose effect would otherwise prove difficult to remove in the spatial domain. Futhermore, analysis of the frequency content of a region of interest is less susceptible than spatial domain analysis to changes in image quality such as overall brightness or altered contrast.[3,4,13]

Automated segmentation of tendinous tissue from the surrounding regions through utilization of the frequency domain has already been implemented by Tuthill et al. in 1999.[18] The procedure involved the rastering of a moving window Fourier transform across the original image, calculating the elliptical major-to-minor axis ratio of the speckle pattern observed in the frequency domain. This approach proved successful in segmentation of healthy tendinous regions when aligned parallel to the ultrasound transducer. However, slight disruptions in the speckle pattern of the tendon caused by probe rotation, motion artifacts generated by the patient or the clinician, or a ruptured tendon led to failed segmentation in the affected regions and frames. The employed segmentation algorithm would therefore readily distinguish between healthy and injured tendinous tissue, but lacks the robustness needed for widespread clinical application due to a dependency on lack of relative motion between transducer and patient as well as transducer angle relative to the pictured tendon. With improvements in parameterization of the defined regions, it may be possible to track the healing stage of a tendon through this approach.[3,8,13,17,18]

Another analysis method implemented in 2008 by Bashford et al utilized frequency analysis of manually defined regions of interest in B-mode ultrasound images as an approach to classify a tendon's potential pathology.[1] The employed algorithm refined the input region by applying a high pass filter to the Fourier transform, suppressing low frequency input that was resulting in a greater misclassification of the tendon by the algorithm. Using multiple parameters and the filtered input, the developed algorithm was able to successfully discriminate between a healthy and injured tendon approximately 80 percent of the time with both inputs. Classification of this algorithm could potentially be improved with the addition of a robust segmentation algorithm to eliminate any possibility of regional effects on classification accuracy, as well as potential correlation of ultrasonic parameters with histological microscopy images obtained through surgical resections during tendon repair.[1,2,7,9,16]

The methods discussed currently rely on parameterization within the frequency domain of a region in order to compare the information contained in the current region of interest to a metric of interest. This process inherently limits the robustness of the system, as comparison with a rigidly defined external comparator generally fails to incorporate compensation for variations in image metrics including quality, overall brightness, degree of saturation, level of contrast, and dynamic range. Furthermore, parameterization of a region into a single value such as elliptical axis ratio may introduce potential for unreliability in situations where the defined parameter fails to capture the intended properties. Direct quantification of similarity between two regions of interest is preferred to prevent reliance on a metric that may be subject to influence from unintended sources.

Computer science applications such as the gesture recognition algorithm utilized in the Xbox Kinect™ sensor apply the concept of distribution matching to successfully quantize the dissimilarity between two compared distributions through calculation of a mutually defined parameter known as the Earth Mover's Distance (EMD). EMD is calculated by computing the effort, along all axes, required to transform one distribution into the other when comparing two distributions. If two distributions can be visualized as a series of hills and valleys, both with normalized mass, the EMD between them is analogous to the total minimum mass than can be moved in the shortest distance to render both distributions identical.

There are many methods for applying boundary rules for flow between the first and final bins; a commonly utilized method allows flow between them, making the assumption that the bins are arranged in a circular or continuous pattern. The value calculated in this manner is called the circular Earth Mover's Distance (cEMD). An example calculation of cEMD is demonstrated in Figure 3.2. Rubner et al. in 1998 demonstrated the effectiveness of EMD as a superior method related to matching perceived similarity and image retrieval applications.[15] Its application in robust hand gesture recognition by Ren et al. demonstrated an impressive 93percent mean accuracy despite increasingly challenging backgrounds, such as poor lighting and cluttered environments.[14]

Because the algorithm centered on calculation of the EMD value for each distribution, the resultant system achieved input rotation invariance, a feature that is equally useful in analysis of medical images. Utilizing cEMD to compare the

dissimilarities of two regions in the frequency domain allows for an understanding of how each entire frequency spectrum compares with the other, yielding a metric that identifies directional consistency in the spatial domain.

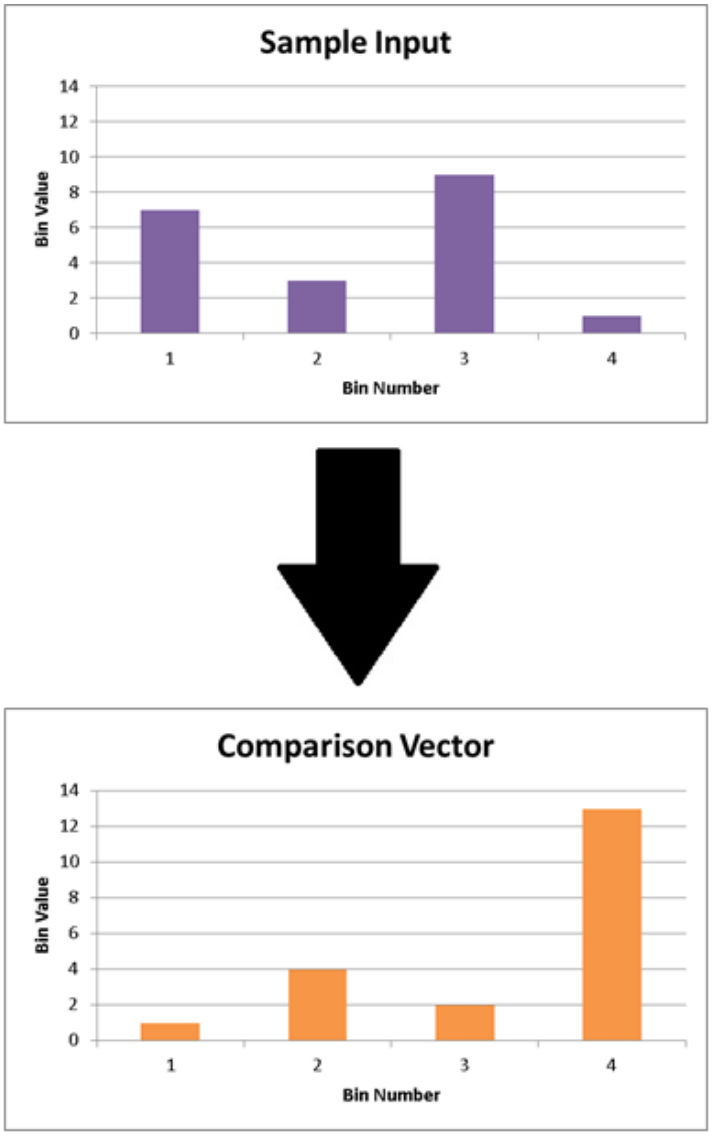

Location	Action	Calculation	Calculation Sum (cEMD)	Result
First Bin Calculation	Move 6 units to Bin 4	6 units*1 distance metric moved = 6	6	First bin balanced, Bin 4 total = 7
Second Bin Calculation	Move 1 unit from Bin 3	1 unit*1 distance metric moved = 1	7	Second bin balanced, Bin 3 total = 8
Third Bin Calculation	Move 6 units to Bin 4	6 units*1 distance metric moved = 6	13	Third bin balanced, Bin 4 total = 13
Fourth Bin Calculation	None	Zero cost	13	Bin 4 balanced

Figure 3.2: Example cEMD calculation shown for two vectors with four bins. Note that for all comparisons of two distributions with equal sums ('mass'), the final bin will always be balanced to the output in the prior step. In this example, the calculated cEMD value between the two distributions is 13, indicating the level of dissimilarity between the compared distributions. Comparing identical distributions yields a cEMD value of zero.

3.3 References

[1] G. Bashford, N. Tornsen, S. Arya, J. Burnfield, and K. Kulig, "Tendinopathy discrimination by use of spatial frequency parameters in ultrasound B-mode images," *Ieee Transactions on Medical Imaging*, vol. 27, pp. 608-615, MAY 2008.

[2] V. Ciriello, S. Gudipati, T. Tosounidis, P. Soucacos, and P. Giannoudis, "Clinical outcomes after repair of quadriceps tendon rupture: A systematic review," *Injury-International Journal of the Care of the Injured*, vol. 43, pp. 1931-1938, NOV 2012.

[3] G. Dougherty, *Digital Image Processing for Medical Applications*. California State University: Cambridge University, 2009.

[4] R. Gonzalez and R. Woods, *Digital Image Processing*, 3rd ed.: Pearson Education, Inc., 2008.

[5] D. HE and W. LI, "Texture Features Based on Texture Spectrum," *Pattern Recognition*, vol. 24, pp. 391-399, 1991.

[6] M. Horng, "Texture Classification of the Ultrasonic Images of Rotator Cuff Diseases based on Radial Basis Function Network," *2008 Ieee International Joint Conference on Neural Networks, Vols 1-8*, pp. 91-97, 2008.

[7] R. James, G. Kesturu, G. Balian, and B. Chhabra, "Tendon: Biology, Biomechanics, Repair, Growth Factors, and Evolving Treatment Options," *Journal of Hand Surgery*, vol. 33A, pp. 102-112, 2008.

[8] T. Khamdaeng, J. Luo, J. Vappou, P. Terdtoon, and E. E. Konofagou, "Arterial stiffness identification of the human carotid artery using the stress-strain relationship in vivo," *Ultrasonics*, vol. 52, pp. 402-11, Mar 2012.

[9] U. Longo, G. Garau, V. Denaro, and N. Maffulli, "Surgical management of tendinopathy of biceps femoris tendon in athletes," *Disability and Rehabilitation*, vol. 30, pp. 1602-1607, 2008.

[10] N. McCormick and J. Lord, "Digital Image Correlation," *Materials Today*, vol. 13, pp. 52-54, 2010.

[11] G. Okotie, S. Duenwald-Kuehl, H. Kobayashi, M. J. Wu, and R. Vanderby, "Tendon strain measurements with dynamic ultrasound images: evaluation of digital image correlation," *J Biomech Eng*, vol. 134, p. 024504, Feb 2012.

[12] B. Pan, K. Qian, H. Xie, and A. Asundi, "Two-dimensional digital image correlation for in-plane displacement and strain measurement: a review," *Measurement Science & Technology,* vol. 20, JUN 2009.

[13] J. Prince and J. Links, *Medical Imaging Signals and Systems*. Upper Saddle River, NJ: Pearson Education, Inc., 2006.

[14] Z. Ren and J. Yuan, "Robust Part-Based Hand Gesture Recognition Using Kinect Sensor," *IEEE Transactions on Multimedia,* vol. 15, pp. 1110-1120, 2013.

[15] Y. Rubner, C. Tomasi, and L. J. Guibas, "A metric for distributions with applications to image databases," *IEEE Conference on Computer Vision,* pp. 59-66, 1998.

[16] P. Sharma and N. Maffulli, "Current concepts review tendon injury and tendinopathy: Healing and repair," *Journal of Bone and Joint Surgery-American Volume,* vol. 87A, pp. 187-202, JAN 2005.

[17] R. G. Spencer, E. F. Calton, and N. P. Camacho, "Statistical comparison of Fourier transform infrared spectra," *J Biomed Opt,* vol. 11, p. 064023, 2006 Nov-Dec 2006.

[18] T. Tuthill, J. Rubin, J. Fowlkes, D. Jamadar, and R. Bude, "Frequency analysis of echo texture in tendon," *Ultrasound in Medicine and Biology,* vol. 25, pp. 959-968, JUL 1999.

CHAPTER IV

TENDINOUS ULTRASOUND IMAGE AND PARAMETER ACQUISITION

4.1 Introduction

Treatment of tendon ruptures and tears is a field that is rapidly growing. With millions of Americans suffering a tendon injury every year, it is important to find a suitable method for properly assessing and managing treatment options while minimizing future risk to the patient.[7] Methods are being developed that involve treatment with growth factors, tissue engineering and gene therapy to improve the healing outcome for tendinous tissue. However, the problem remains that it is difficult to determine the stage of healing and mechanical properties of the tendon *in vivo*. These solutions provide improved healing rates for tendons, but fail to provide superior insight into the stage of healing an injury has progressed to or the mechanical properties of the injured tendon. These shortcomings drive the need for development of a model capable of predicting the mechanical properties of a tendon imaged *via* ultrasound modalities through parameterization of tendinous regions.

Use of texture mapping to distinguish between tendons of different mechanical properties is a promising application of image processing to build a model helpful for diagnosis. The combination of these two elements will help us produce a predictive model that will show the limits of the healing tendon. Ultrasound is a highly portable and easy to use technology. This type of predictive model would be extremely useful to combat medics who need to diagnose tendinous injuries in the field. This method could

also allow a physician or physical therapist to determine the maximum amount of force they can apply to the tendon before it will rupture. Ultimately, this ability will lead to reduced therapy times and reduced patient discomfort by allowing for maximum movement during therapy while preventing overloading and recurrence of injury.

Currently, ultrasonic imaging techniques can be used to measure arterial stiffness and mechanics in vivo.[1,4,8,9,14] These methods allow for advantageous non-invasive determination of a vessel's mechanical properties that enhance clinical diagnostics. Arterial incremental displacements can be determined using a 1-D cross-correlation method comparing each frame.[9] Similarly, ultrasonic imaging is used in the clinic for diagnostic purposes regarding tendons. Generally, diagnosis is performed by a physician's eye observations, although ultrasound image analysis methods have now been demonstrated to properly classify tendon injury type with approximately 85% accuracy.[6]

A variety of ultrasonic image parameters may be utilized to evaluate a tendon's properties, including digital image correlation, central symmetry, and spatial frequency analysis.[2,3,5,6,10,11,12,13,15] The method selected for use in the developed program will be determined by analysis of each method's computation time and strength of correlation to experimental data. Figure 4.1 shows example ultrasonic supraspinatus images containing diseased tissues that can be classified using these techniques. The ability to correlate tendon ultrasonic image parameters used in texture analysis with a tendon's mechanical properties and histological composition will result in a powerful tool for assisted diagnostics.

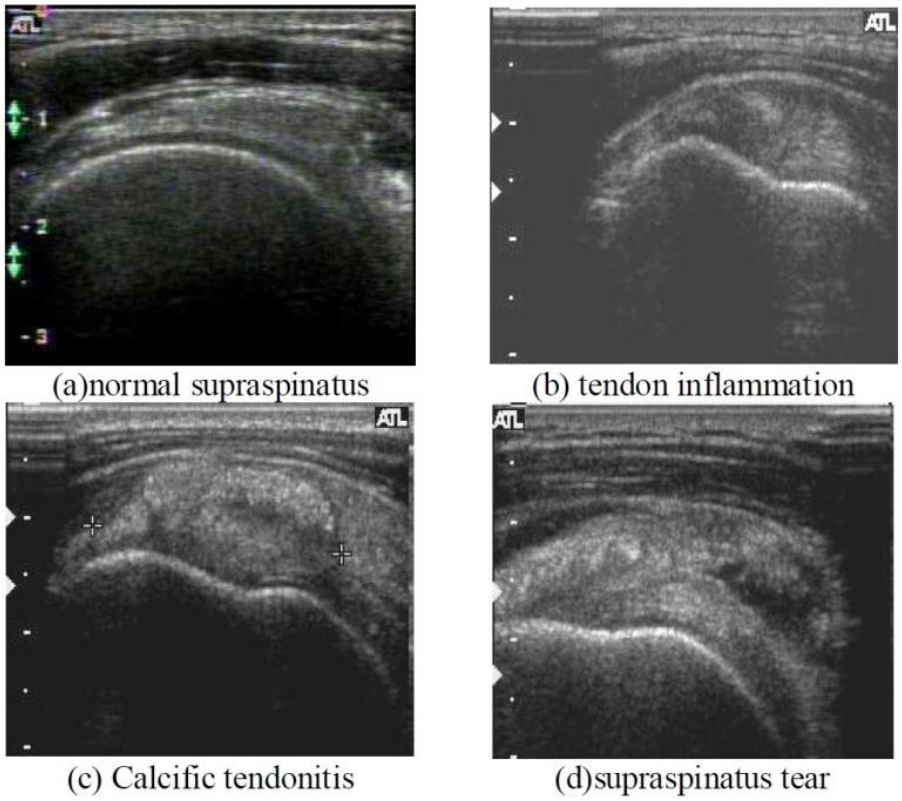

Figure 4.1: Samples of ultrasonic supraspinatus images. The image (a) is a normal case, image (b) is a sample of tendon inflammation. The images (c) and (d) are calcific tendonitis and tear, respectively (Adapted from [6] Horng et al.)**.**

4.2 Materials and Methods

4.2.1 Ultrasound Image Acquisition and Preparation

B-mode ultrasound images were obtained using a Philips IU-22 Ultrasound System at the Clemson University Biomedical Engineering Innovation Campus (CUBEInC). Ultrasonic procedure was completed adhering to Philips guidelines for ultrasonography of the knee (printed in USA G64215 6-03), outlined in this section.

Before and during image acquisition, considerations were given for the following conditions:

- Patient position
- Transducer orientation
- Joint position
- Dynamic flexion-extension of the knee
- Scanning plane

During the imaging process, the patient's knee was held at approximately 90 degrees. Anterior probe positioning was required in order to visualize the patellar tendon along its longitudinal axis. For comparison, a transverse image of the patellar tendon was obtained in a separate output by a rotation of the probe 90 degrees from its original orientation. Probe orientation was always implemented such that the clinical standard image alignment was observed; that is, the top of the ultrasound image always corresponded to the superior or medial position. The transducers for which images were acquired were the Philips L9-3 and L15-7io models. A male and female volunteer allowed for obtainment of five sets of images: Female Longitudinal Axis L9-3 (FLL93), Female Longitudinal Axis L15-7io (FLL157io), Male Transverse Axis L9-3 (MTL93), Male Longitudinal Axis L9-3 (MLL93), and a second data set obtained on a different date for Male Longitudinal Axis L9-3 (ML2L93), for comparison.

Once obtained, a time series of approximately 650 B-mode images were compiled into a dicom file and saved for output in each case. The files were transferred to a portable hard drive for further processing in Matlab® (MathWorks). Figure 4.2 demonstrates a representative frame for each of the transducers used. Further examples are available in Appendix A. Before further analysis could be completed, the image was

cropped to remove the banner and border regions shown. Further analysis was conducted on the resultant series of images for each dicom set.

Figure 4.2: Representative images of the patellar tendon obtained from the Philips IU-22 Ultrasound System. Top: A longitudinal view of the female patellar tendon visualized with the L15-7io probe, resulting in a comparatively smaller domain with higher resolution. Bottom: A longitudinal view of the male patellar tendon visualized with the L9-3 probe. Note that the larger domain results in lower resolution. Image depth is displayed at the bottom right of each image, in centimeters.

4.2.2 Ultrasound Image Texture Analysis

Once imported into Matlab, each dicom set was reviewed in order to remove any large sections of gross motion artifacts due to probe movement relative to the patient. This was necessary in some cases due to the length of the interval in which 650 consecutive images were acquired, causing unintended motion. After removal of frames lost due to motion artifacts, the first frame was displayed to the user for selection of the region of interest. For each set, four regions were selected. Two regions were outlined of the patellar tendon and superficial background tissue each. In each case, an iteration of the script was run for a large region and a small region, the latter of which was intended to further reduce the effects of motion artifacts by identifying and selecting regions in which view artifacts were observed. The tissue superficial to the patellar tendon was selected in every case to represent all background tissue in order to maintain consistency in addition to representing the region most similar to the patellar tendon. Each region was identified by the user on the first frame using the roipoly function within Matlab, and was used for calculations on all frames for the dicom set in which it belonged. Examples of each region selection method are shown for one frame in Figure 4.3. For clarity, further examples are shown in Appendix B. Examples shown will be displayed for the first frame of the FLL157io data set when relevant.

For the purposes of calculation, each frame's values were then normalized to a range of zero and one. The gray-level co-occurrence matrix (GLCM) was then calculated for the highlighted region, and entropy values calculated from the probability density function (PDF) and GLCM were stored in an output structure for each frame. The means

and standard deviation of each category for every dicom set were later calculated for comparison. In order to maintain consistency with the data available for techniques in Chapter 5, only those frames for which a complete data set was available were used in these calculations.

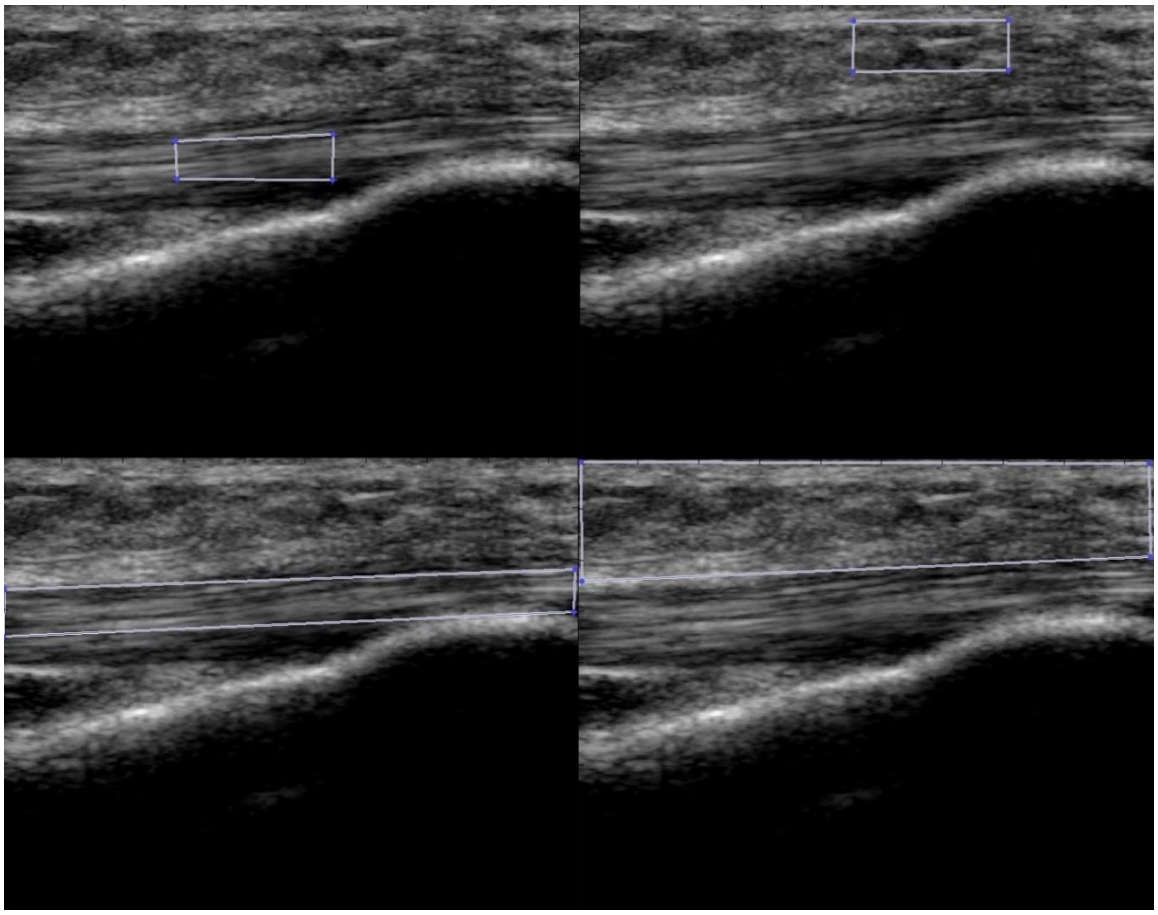

Figure 4.3: Example region of interest selection for each iteration of the Matlab script per frame. Top left: Small region selected of the patellar tendon. Top right: Small region selected of the superficial background. Bottom left: Large region selected of the patellar tendon. Bottom right: Large region selected of the superficial background.

4.3 Results

4.3.1 Small Region Entropy Calculation

Entropy means for the small region selection are shown in Figures 4.4 and 4.5,

respectively. All calculations were completed in Matlab, and the data were transferred to Excel® spreadsheets for later reference. The entropies derived from the PDF are orders of magnitude lower than those calculated from the GLCM: this is due to the normalization step taken for the PDF matrix, where the GLCM contains a sum equal to the number of pixels in the region.

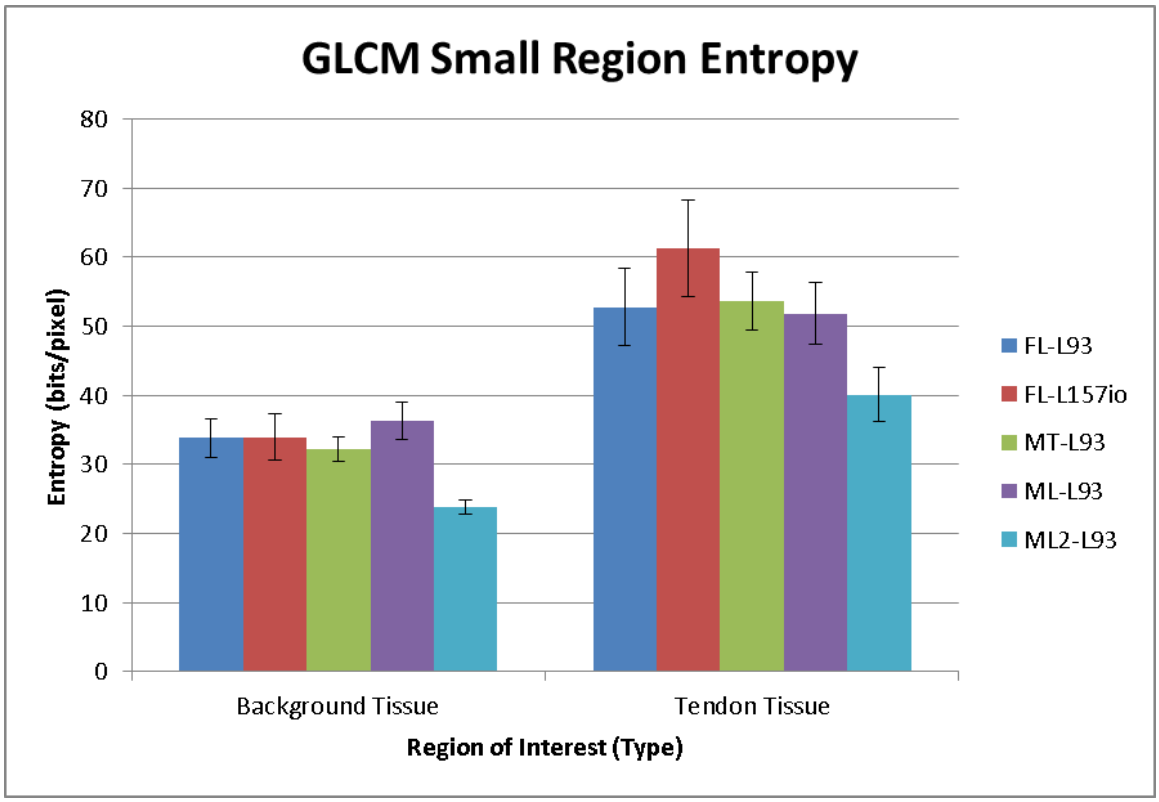

Figure 4.4: Entropy means calculated for each dicom set from the GLCM derived from the small input regions.

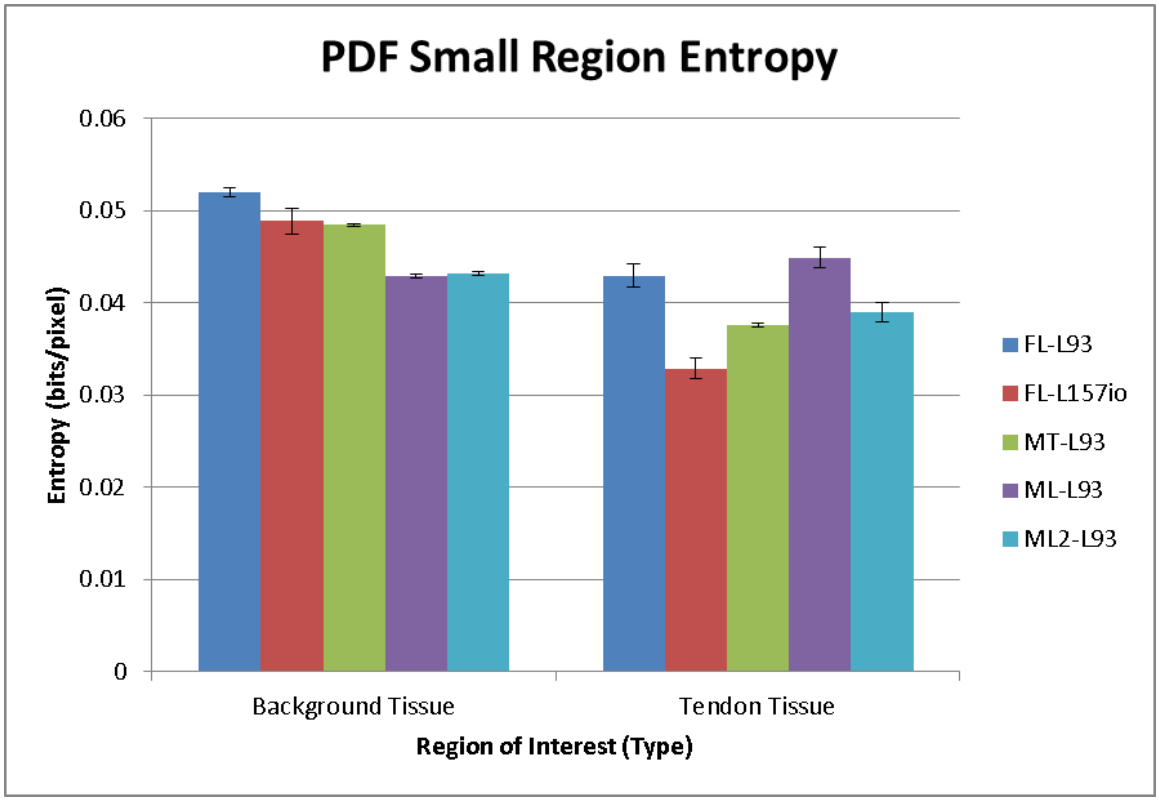

Figure 4.5: Entropy means calculated for each dicom set from the PDF matrices of the small input regions.

Regarding the GLCM-derived Entropy, background tissue entropy primarily centered around 30 bits/pixel. The lowest background entropy value was derived from ML2L93 at under 24 bits/pixel. All mean values computed for background regions fell below those for tendinous regions. For the tendinous entropy means, ML2L93 again displayed the lowest entropy value at approximately 40 bits/pixel. No other tendinous entropy mean calculated from the GLCM small region selection fell below 50 bits/pixel. The greatest difference in entropy mean difference between regions was established by FLL157io with a difference of over 27 bits/pixel. Least significant was the difference in magnitude between the ML2L93 regions, which were separated by 16.3 bits/pixel.

Results derived from the PDF matrix were somewhat more varied; the distributions of magnitudes overlapped. In general, however, the relationship between region of interest and mean entropy value was reversed. For all but MLL93, background tissue mean entropy calculated with small region selected exceeded that of its corresponding tendinous mean entropy value. The largest discrimination between regional mean entropy values was again FLL157io, with a 0.016 bits/pixel difference, a 32 percent decrease. Most closely related were the MLL93 values, separated by 0.00197 bits/pixel.

4.3.2 Large Region Entropy Calculation

Entropy means calculated using the large region selection method are shown in Figures 4.6 and 4.7 for GLCM and PDF origins, respectively. The relationship between the relative magnitudes of background mean entropy and tendinous mean entropy when calculated using the GLCM large region selection were reversed from the paradigm observed with the GLCM small region method. No tendinous mean entropy calculated using the GLCM large region exceeded its corresponding background mean entropy of the same method. Some overlap between their distributions of magnitudes was observed for the male data sets.

The smallest difference in entropies calculated was for MLL93 at 6.9 bits/pixel, just a 5.4 percent change. The largest magnitude change was manifested by FLL157io, with 253 bits/pixel corresponding to a 72 percent decrease in magnitude between background and tendinous regions. Magnitudes for mean entropy calculated from the PDF large region method were tightly clustered: only one value across all regions was

computed to not be within 0.012 and 0.014 bits/pixel. That value was 0.0155 bits/pixel for the tendinous region of MTL93.

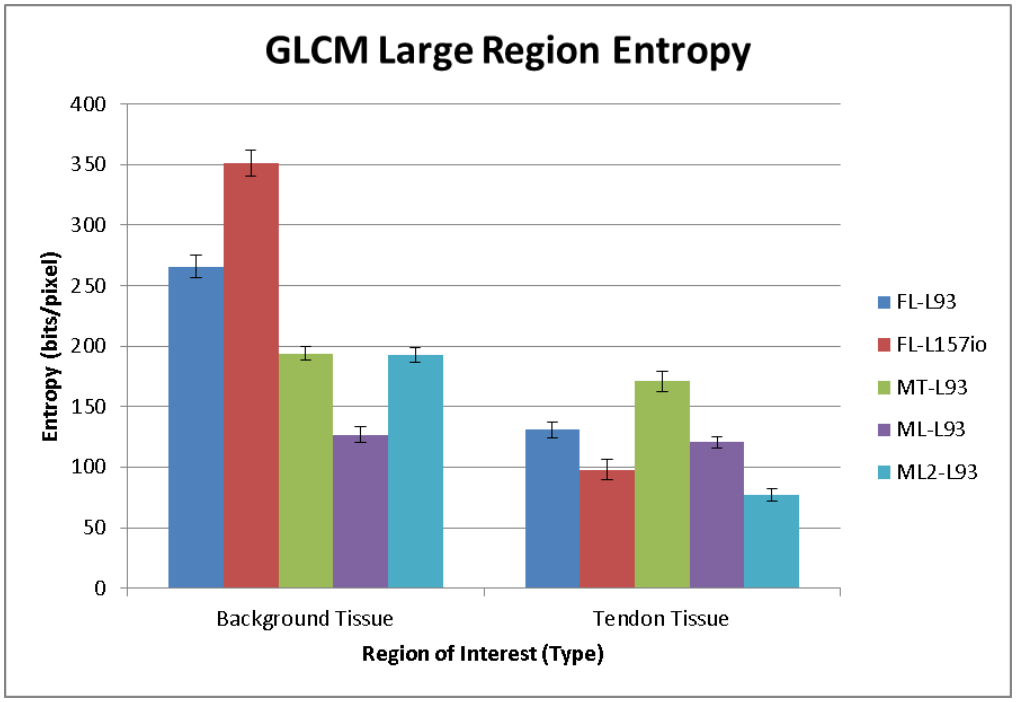

Figure 4.6: Entropy means calculated for each dicom set from the GLCM of the large input regions.

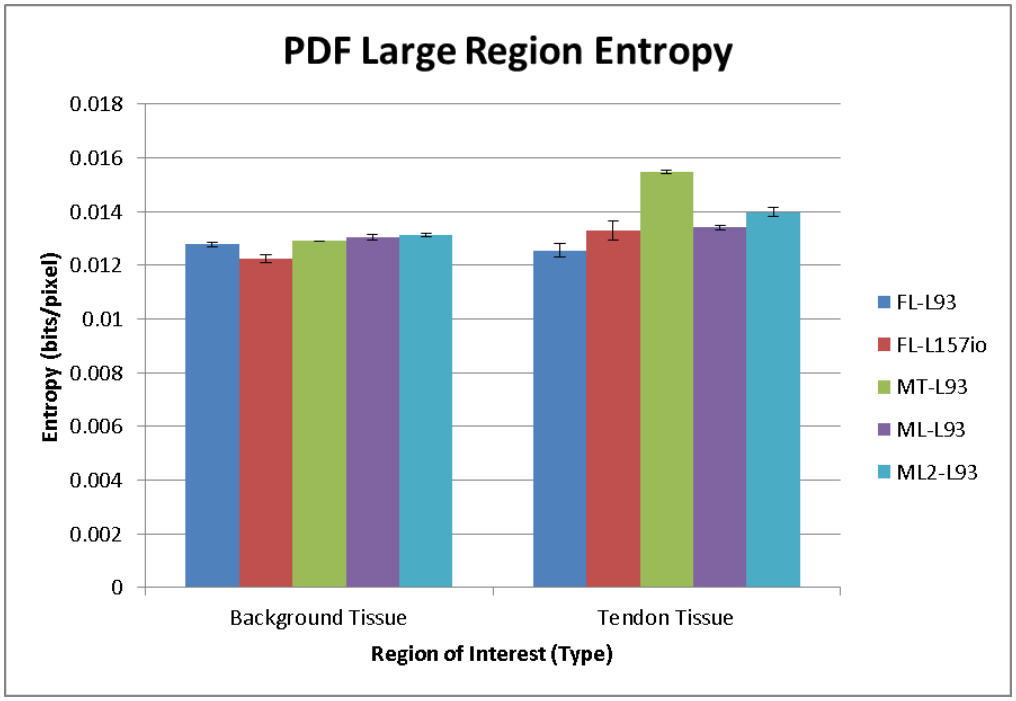

Figure 4.7: Entropy means calculated for each dicom set from the PDF matrices of the large input regions.

4.4 Discussion

While the results seem to indicate contradictory paradigms in some cases, sound understanding of the basis behind the results reveals consensus among the methods used. There is an apparent pattern shift between the GLCM small region method and the GLCM large region method. However, observation during the data acquisition phase indicated that the small region method, in particular the background tissue calculations, varied dramatically with relatively small changes in region selection. This is likely due to the large number of tissue borders in the superficial background region; not only do these borders often separate regions of contrasting properties, but the presence of the borders themselves has a significant impact on entropy calculations. Consequently, true representation of a region through entropy calculations is only feasible if the region is relatively homogeneous.

Regarding mean entropy calculation derived from the probability density function, the observed result was expected. Spatial organization has no impact on the probability density function; this is best demonstrated in the large region entropy calculation, which demonstrates almost total uniformity of entropy across probe type, patient gender, and tissue type. The comparatively larger variations in the small region method are likely a result of sampling bias due to the inherently smaller area collected for calculation. As a means for reducing the impact of motion artifacts in the parameterization, small region sampling has demonstrated too many drawbacks to be advantageous.

The effect of motion artifacts on the large region method may still be unclear.

Once again due to its spatial independence, entropy derived from the PDF is relatively unaffected by motion artifacts; provided the distribution of pixel intensity is similar, the PDF will remain unaffected. The effect of motion artifacts on the large region, GLCM-derived entropy values is less certain. Almost all male dicom sets possessed very similar entropy to one another, and little distinction between background tissue and tendinous tissue was evident for MTL93 and MLL93. While the different tissue types became somewhat more pronounced with ML2L93, the most dramatic difference was displaying in FLL157io, possibly due to the transducer's superior resolution. If such a distinction does exist between background and tendinous tissues, the smaller differences visible with the L9-3 probe may be obscured by the confounding nature of motion artifacts. While interference from motion may be affecting the entropy calculations in the large region method, the robustness to local variations in tissue structure results in greater stability that is too substantially impacted in the small region method.

4.5 Conclusion

The small region method has proven to have an overall negative impact on the reliability of parameterization of the ultrasound image. However, reduction of the impact of motion artifacts remains a concern when selecting large tissue regions during processing. Entropy as an indicator of tissue texture revealed promising results that demonstrate its potential for future parameterization of ultrasound regions.

Identification of tissue borders and automated segmentation would improve the performance of entropy as a diagnostic aid for tendinous injuries. Texture comparison of

healthy and injured tendons is needed for the future in order to establish the effectiveness of such an approach. Future work will address these needs as well as the need for implementation of a registration process in order to reduce the effect of motion artifacts.

4.6 Acknowledgements

I would like to acknowledge my advisor, Dr. Dean, for mentoring me and offering guidance every time I needed it. I would also like to acknowledge my committee member, Dr. Kwartowitz, for teaching me proper use of ultrasound systems and exercising patience while I learned. Additionally, I would like to thank Heather Woodward for her patience in traveling and volunteering for image acquisition.

4.7 References

[1] G. Bambi, T. Morganti, S. Ricci, E. Boni, F. Guidi, C. Palombo, *et al.*, "A novel ultrasound instrument for investigation of arterial mechanics," *Ultrasonics,* vol. 42, pp. 731-737, APR 2004

.

[2] G. Bashford, N. Tornsen, S. Arya, J. Burnfield, and K. Kulig, "Tendinopathy discrimination by use of spatial frequency parameters in ultrasound B-mode images," *Ieee Transactions on Medical Imaging,* vol. 27, pp. 608-615, MAY 2008.

[3] J. Collinger, D. Gagnon, J. Jacobson, B. Impink, and M. Boninger, "Reliability of Quantitative Ultrasound Measures of the Biceps and Supraspinatus Tendons," *Academic Radiology,* vol. 16, pp. 1424-1432, NOV 2009.

[4] A. Danpinid, J. Luo, J. Vappou, P. Terdtoon, and E. Konofagou, "In vivo characterization of the aortic wall stress-strain relationship," *Ultrasonics,* vol. 50, pp. 654-665, JUN 2010.

[5] Y.-C. Du, Y.-F. Chen, C.-E. Yang, Y.-Y. Lee, T. Chen, and C.-H. Chang, "Measurements of Stress-Strain Properties of Tendon with Ultrasound Parameters," in *International Federation for Medical & Biological Engineering*, Singapore, 2010, pp. 930-933.

[6] M. Horng, "Texture Classification of the Ultrasonic Images of Rotator Cuff Diseases based on Radial Basis Function Network," *2008 Ieee International Joint Conference on Neural Networks, Vols 1-8,* pp. 91-97, 2008.

[7] R. James, G. Kesturu, G. Balian, and B. Chhabra, "Tendon: Biology, Biomechanics, Repair, Growth Factors, and Evolving Treatment Options," *Journal of Hand Surgery,* vol. 33A, pp. 102-112, 2008.

[8] A. Kamenskiy, Y. Dzenis, J. MacTaggart, T. Lynch, S. Kazmi, and I. Pipinos, "Nonlinear Mechanical Behavior of The Human Common, External, and Internal Carotid Arteries In Vivo," *Journal of Surgical Research,* vol. 176, pp. 329-336, JUL 2012.

[9] T. Khamdaeng, J. Luo, J. Vappou, P. Terdtoon, and E. Konofagou, "Arterial stiffness identification of the human carotid artery using the stress-strain relationship in vivo," *Ultrasonics,* vol. 52, pp. 402-411, MAR 2012.

[10] P. Li, P. Kuo, C. Shun, S. Schneider, M. Levy, and B. McAvoy, "Ultrasonic strain measurements of tendon," *1999 Ieee Ultrasonics Symposium Proceedings, Vols 1 and 2,* pp. 1661-1664, 1999.

[11] M. Lu, Y. Zheng, H. Lu, Q. Huang, and L. Qin, "Evaluation of Bone-Tendon Junction Healing Using Water Jet Ultrasound Indentation Method," *Ultrasound in Medicine and Biology,* vol. 35, pp. 1783-1793, NOV 2009.

[12] L. Meershoek, A. van den Bogert, and H. Schamhardt, "Model formulation and determination of in vitro parameters of a noninvasive method to calculate flexor tendon forces in the equine forelimb," *American Journal of Veterinary Research,* vol. 62, pp. 1585-1593, OCT 2001.

[13] G. Okotie, S. Duenwald-Kuehl, H. Kobayashi, M. J. Wu, and R. Vanderby, "Tendon strain measurements with dynamic ultrasound images: evaluation of digital image correlation," *J Biomech Eng,* vol. 134, p. 024504, Feb 2012.

[14] A. Reddy, S. Madala, A. Jones, W. Caro, J. Eberth, T. Pham, *et al.*, "Multichannel Pulsed Doppler Signal Processing for Vascular Measurements in Mice," *Ultrasound in Medicine and Biology,* vol. 35, pp. 2042-2054, DEC 2009.

[15] T. Tuthill, J. Rubin, J. Fowlkes, D. Jamadar, and R. Bude, "Frequency analysis of echo texture in tendon," *Ultrasound in Medicine and Biology,* vol. 25, pp. 959-968, JUL 1999.

CHAPTER V

SEGMENTATION OF TENDONS IN B-MODE ULTRASOUND

5.1 Introduction

As discussed in Chapter 4, segmentation of tendinous regions in ultrasonic images offers great potential for improving the performance of parameterization in digital processing. Considering as much of a region of interest as possible offers robustness against common forms of interference, such as motion artifacts and local variations of intensity and texture.[2,6] Functional tendon segmentation along the longitudinal axis of superficial, parallel tendons has already been implemented.[7] However, there is a need in this application for a segmentation algorithm that is robust to probe rotation, angle, and tendon orientation and shape.[1,4,5] Proper identification of a tendinous region allows for specialized parameterization reliant on the assumption that contributing pixels all fall within a tendinous region, as with speckle pattern analysis and comparison to a radial basis function network.[4,7] Processes reliant on texture analysis, such as entropy computations, applied over a domain larger than the region of interest lose sensitivity and accuracy as the region of interest's contribution to the total area decreases. Consequently, successful distinction of a tendon from surrounding tissue is closely associated with improved feature extraction.

The circular Earth Mover's Distance (cEMD) calculation discussed in Chapter 3 offers a robust method for comparing two total distributions. It is anticipated that clever implementation of this ability will allow for discrimination of regions in B-mode ultrasound based on directional consistency. Though cEMD calculations offer a robust

method for comparison of two distributions, it suffers from substantial computation requirements.[3] Use as a real-time segmentation process would therefore involve significant advances in its optimization.

5.2 Materials and Methods

Several of the dicom files discussed in Chapter 4 were utilized for assessment of the segmentation algorithm. For clarity, figures displayed will consist of a single FLL157io frame when relevant. Further examples are available for browsing in Appendices A through D.

Due to the computation time required per frame, the imported dicom files were sampled such that the collected frames were equally separated throughout the entire original series. The number of acquired frames approximated 35 for all but one file, for which the number of acquired frames totaled 134. For each file, a mask consisting of a small 16 by 16 region was defined on the first frame that would later be used to as a representative tendinous region against which comparisons could be made.

5.2.1 Moving Window Fourier Transform and Tendon Mask Comparison

A cEMD for each interior pixel in the original image was computed in the following manner:

- The Fourier Transform of the 16 by 16 pixel mask, defined by the user, is calculated.
- A moving window (16 by 16 pixels), whose current position is defined as the center pixel, rasters through the image, column by column, row by row.

- For each interior pixel, the Fourier Transform of the moving window is calculated.
- Each two dimensional Fourier Transform is converted to one dimension by a phase angle energy summation: The sum of the squares of the elements in each half quadrant (45 degrees) is calculated and stored in an eight element vector.
- The cEMD value defined for that pixel is the cEMD calculated for the mask and current window.

This process is shown graphically in Figures 5.1 and 5.2. When an interior pixel is reached, the script calculates the Fourier Transform of the local window, converts it to a one dimensional vector through an energy summation, shown in Figure 5.2, and computes the cEMD between that pixel's vector and the mask vector.

In addition to defining a cEMD value for each interior pixel, the moving window's mean intensity and Discrete Laplacian (as an indicator of intensity variance in the region) were stored for each interior pixel as well. These calculations are repeated until the final interior pixel has been assigned its three parameters.

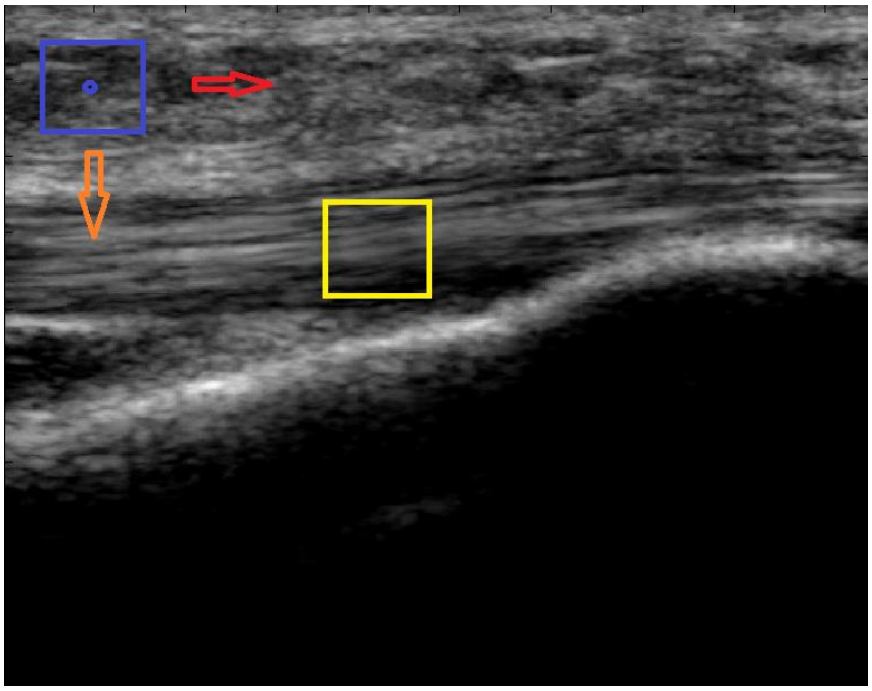

Figure 5.1: Mask and raster process of the Matlab script. Yellow Box: An example of a mask region selected by the user, sampling tendinous tissue for comparison. Blue Box: Example local region defined for a particular interior pixel. Blue Circle: Particular pixel for which the blue box region is defined. Red Arrow: When proceeding to the next pixel, the script rasters first along the red arrow direction. Orange Arrow: After completing a row of calculations, the script then rasters one pixel along the orange arrow direction and continues.

Figure 5.2: Map of the Fourier Transform of a 16 by 16 pixel window. Elements of the same color and text are individually squared, then summed, to yield an energy value for each phase angle. Bins begin with the zero to 45 degree Q1- blue section and continue counterclockwise until the final 315 to 360 degree Q4+ black section. Note that the first and final bins are adjacent to one another; this is why the circular Earth Mover's condition is valid.

5.2.2 Calculation of Local Comparison cEMD

After all interior pixels have an energy vector of their Fourier Transform defined, a second pass through the frame is conducted to calculate the cEMD values of each pixel's vector as it relates to some of its neighbors. To observe the effect of pixel separation and number of vectors in all eight primary directions, a series of such calculations were conducted for each pixel. Observed quantities included one pixel separation paired with 16 regions in all eight directions, four pixel separation paired with eight regions, eight pixel separation paired with four regions, and 16 pixel separation paired with two regions. For a given method pair, the individual cEMD values were combined in two ways, for comparison: a standard mean, and a Gaussian weighted average centered on the pixel of interest. The result of this method is eight further cEMD average values that are defined for each interior pixel. Due to region size and comparison to adjacent regions, more border values could not be calculated. However, the bulk of pixel values remained fully defined.

5.3 Results

A comparison of the example image, its mean intensity map, its Discrete Laplacian, and a map of the cEMD values calculated with respect to the user defined mask is shown in Figure 5.3. Results across different dicom sets were fairly consistent; more examples are available in Appendix C.

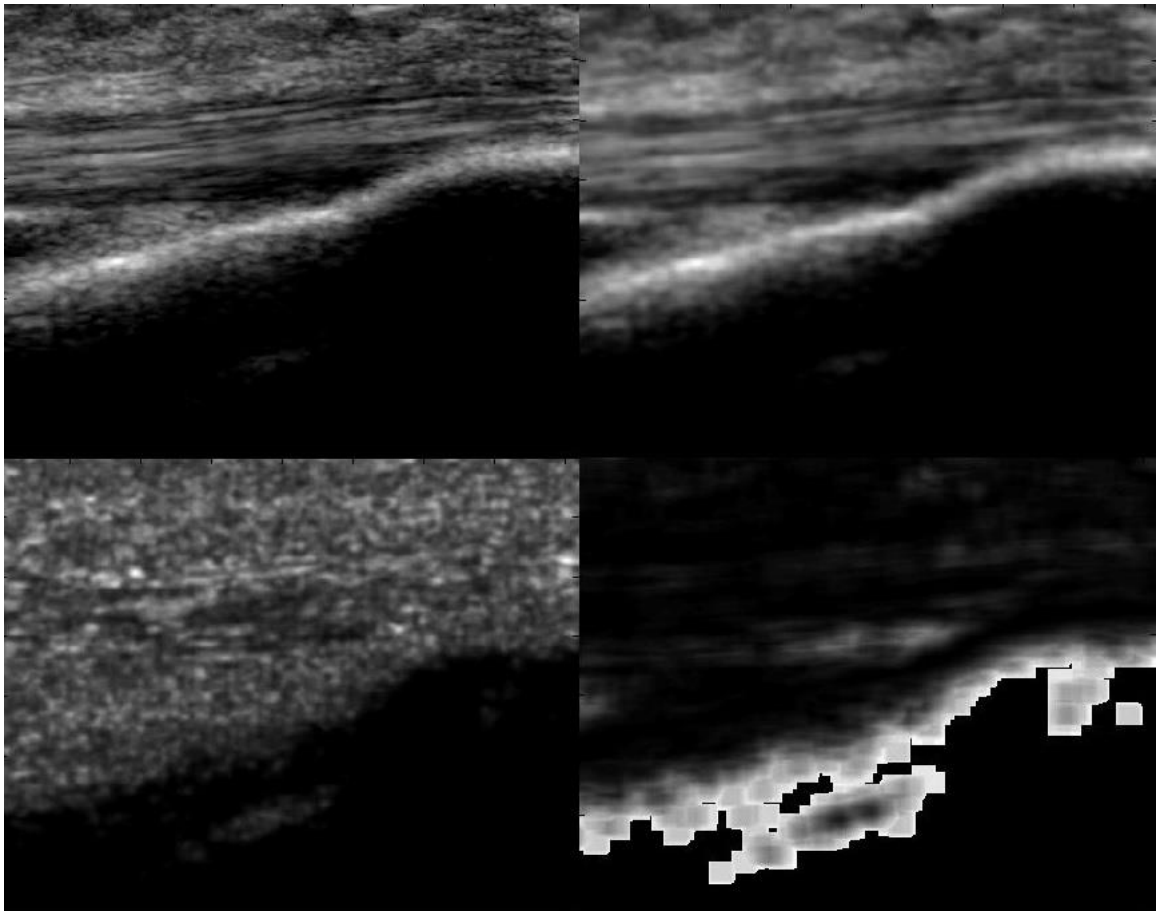

Figure 5.3: Comparison of the original image with the defined parameter values. Top left: Original image. Top right: Mean intensity image. Bottom left: Discrete Laplacian. Bottom right: cEMD relative to the user defined tendinous mask.

The mean intensity calculation results in a blurring effect on the original image; this is mathematically equivalent to the process of averaging local intensities for output. The Discrete Laplacian demonstrated a large speckle pattern for non-zero inputs. Some elongation of this speckle pattern can be observed in the tendinous region. The mask cEMD values varied significantly in magnitude. The tibial interface with the surrounding tissue resulted in very large cEMD values orders of magnitude above other regions, indicating a very large discrepancy in the spatial frequency pattern of the tendon and bone. The zero input regions beyond the tibial surface resulted in zero output matrices;

values of zero must be excluded before any minimization procedure can be performed on the cEMD values.

Results for the local comparison cEMD values calculated in the second pass of each image are shown in Figures 5.4 and 5.5 for standard mean and Gaussian weighted average, respectively. Due to the large range of values calculated for the cEMD, the base 10 logarithm of each image is shown for clarity. Figure 5.4 displays all standard mean calculations in addition to their logarithms. Figure 5.5 compares one logarithm of a standard mean calculation with its related Gaussian average. Among all Gaussian and standard mean cEMD matrices, few differences were noted. Discontinuities in the image were increasingly observed with less overlap among compared regions, and contrast was, in general, greater for the greatest overlap of regions. Additional examples of Gaussian and standard mean cEMD matrices are provided in Appendix D.

Figure 5.4: Standard mean cEMD images. The left column displays the original matrices; the right column illustrates their respective base 10 logarithms. Pictured from top to bottom: One pixel separation, 16 regions in each direction; four pixels separation, eight regions in each direction; eight pixels separation, four regions in each direction; 16 pixels separation, two regions in each direction.

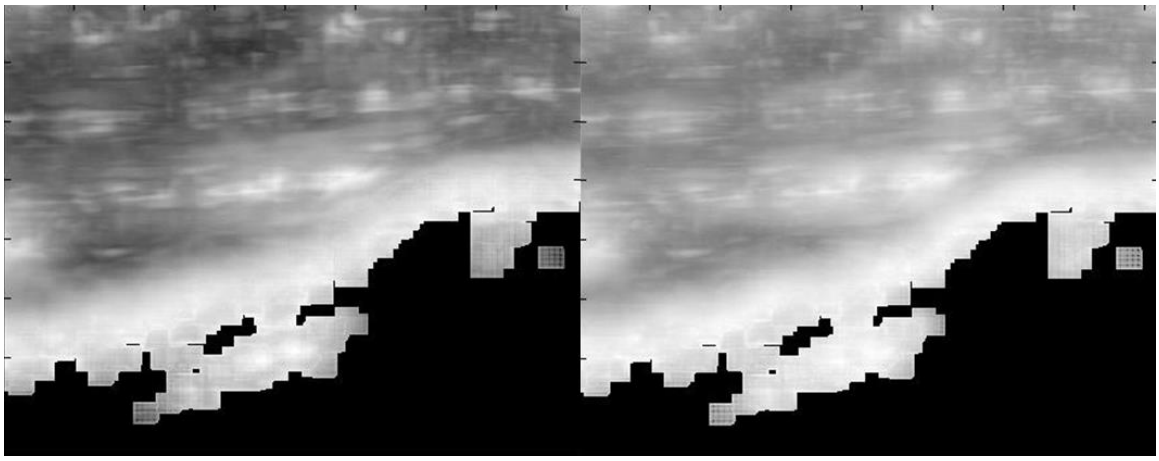

Figure 5.5: Comparison of standard mean and Gaussian averaging methods for four pixel separation, eight regions in each direction sampling method. Left: Standard mean method. Right: Gaussian weight average method.

Results displayed previously include several calculations based on a single frame. In addition, the effects of pointwise averaging of the cEMD results were observed. Averaging was completed using a sampling of the dicom set with zero separation between frames. This was necessary to ensure the correct function of the image registration algorithm used to reduce motion artifacts in the output. Figure 5.6 shows the effect of particular forms of averaging on the local region cEMD matrix. For these studies, a Gaussian weighted average employing the four pixels, eight regions in each direction method for cEMD calculations.

Time averaging of the cEMD had the effect of smoothing on the output matrix. Motion artifacts appeared to have little effect on this dicom set on the time scale of 60 frames; little difference was observed for the output with and without motion correction. An average of just two frames of the cEMD displayed a noticeable effect on the contrast in the output image. A pointwise multiplication of the mean intensity with the Discrete Laplacian scaled the Discrete Laplacian relative to the local intensity values in each

region. The output matrix of this operation demonstrates this principle: areas of very low intensity became very dark on the combined metric output. Output intensity appeared to scale primarily with mean intensity, with a secondary effect associated with the Discrete Laplacian.

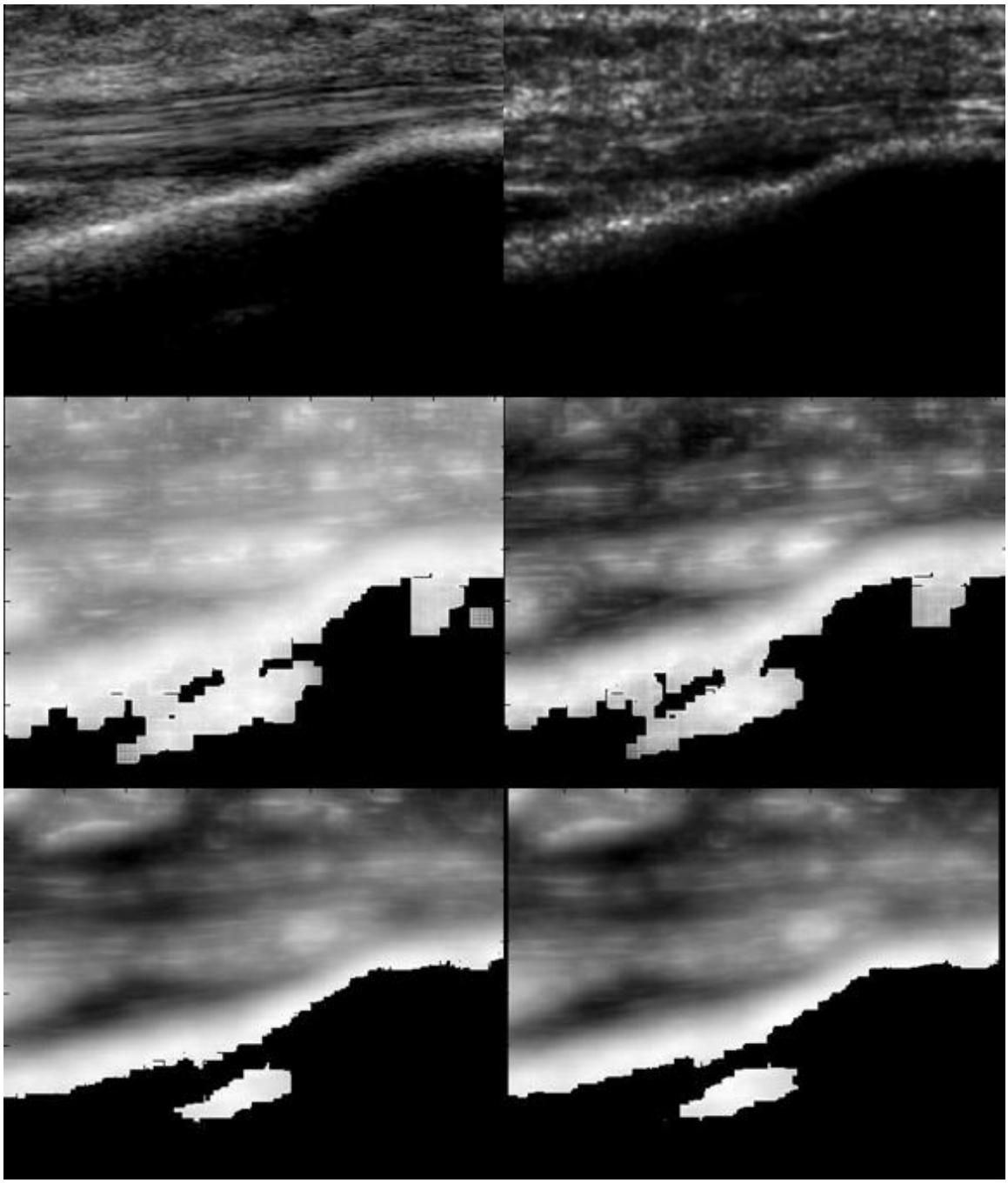

Figure 5.6: Effects of time averaging on the Gaussian weighted cEMD. Top left: Original image. Top right: Pointwise product of the Discrete Laplacian and mean intensity parameters. Middle left: Base 10 logarithm of the Gaussian weighted average cEMD for the original image. Middle right: Base 10 logarithm of the Gaussian weight average cEMD as a pointwise product of the first two frames. Bottom left: Base 10 logarithm of the pointwise average of the first 60 frames in the FLL157io dicom set without motion correction. Bottom right: Base 10 logarithm of the pointwise average of the first 60 frames in the FLL157io dicom set with motion correction.

5.4 Discussion

Results for the cEMD calculations do appear lower in the tendinous regions, but also return values of approximately equal value for other regions of the image with directional consistency as well. This limits its current use for the segmentation of tendinous regions until further improvements to the algorithm can be made. Time averaging did show some potential as a smoothing process, after which a post-process application of a series of erosion and dilation iterations may yield features for which identification of the tendinous region is possible. Compiling the mean intensity, Discrete Laplacian, mask cEMD values, and local directionality cEMD values into a single metric in a logical and effective way is both highly desirable and non-trivial. Magnitudes of each parameter not only vary on dramatically different scales, but identify tendinous regions in very different ways. The patellar tendon is a hyperechoic structure in ultrasound, resulting in a comparatively high mean intensity. Minimization of the cEMD matrix is desired in order to locate the most closely related match.

5.5 Conclusion

The current state of the proposed segmentation algorithm is unable to reliably isolate tendinous regions as intended. However, the possibility for improvement is substantial and with application of appropriate steps in the future, a robust segmentation algorithm for tendinous regions could be created. Time averaging of the cEMD matrix and its smoothing effects appeared to highlight the borders of the tendon sheath, separating the low values of the tendon from low values of adjacent regions. With the

proper application of shape priors or assumptions of image configuration, isolation of the tendon in this way is achievable.

Future work should strive to improve the sharpness of the cEMD matrices; current iterations of this algorithm display too much noise to offer sharply defined borders. Additionally, identification of a properly defined single metric incorporating input from the mean intensity, Discrete Laplacian, mask cEMD values, and local cEMD values represents a goal that, if achieved, could substantially improve the quality of image outputs.

5.6 Acknowledgements

I would like to thank my advisor, Dr. Delphine Dean, and my committee members, Dr. Brian Dean and Dr. David Kwartowitz, for their guidance and support during my studies. I would also like to thank Mr. Chris Hawkins for his help developing the Matlab script and output formatting. Furthermore, I would like to acknowledge the following people for volunteering to help complete all the computations necessary for this study: Mr. Hunter Pelham, Mr. Jacob Addison, and Mr. William James.

5.7 References

[1] V. Ciriello, S. Gudipati, T. Tosounidis, P. Soucacos, and P. Giannoudis, "Clinical outcomes after repair of quadriceps tendon rupture: A systematic review," *Injury-International Journal of the Care of the Injured,* vol. 43, pp. 1931-1938, NOV 2012.

[2] G. Dougherty, *Digital Image Processing for Medical Applications*. California State University: Cambridge University, 2009.

[3] R. Gonzalez and R. Woods, *Digital Image Processing*, 3rd ed.: Pearson Education, Inc., 2008.

[4] M. Horng, "Texture Classification of the Ultrasonic Images of Rotator Cuff Diseases based on Radial Basis Function Network," *2008 Ieee International Joint Conference on Neural Networks, Vols 1-8,* pp. 91-97, 2008.

[5] U. Longo, G. Garau, V. Denaro, and N. Maffulli, "Surgical management of tendinopathy of biceps femoris tendon in athletes," *Disability and Rehabilitation,* vol. 30, pp. 1602-1607, 2008.

[6] J. Prince and J. Links, *Medical Imaging Signals and Systems*. Upper Saddle River, NJ: Pearson Education, Inc., 2006.

[7] T. Tuthill, J. Rubin, J. Fowlkes, D. Jamadar, and R. Bude, "Frequency analysis of echo texture in tendon," *Ultrasound in Medicine and Biology,* vol. 25, pp. 959-968, JUL 1999.

CHAPTER VI

RECOMMENDATIONS

The parameterization and segmentation methods explored offer significant potential in the application of tendinous region isolation and analysis. Before that potential can be fully realized, improvement on the implementation of parameterization during the segmentation process is necessary. Specifically, a single segmentation output dependent on all parameters defined represents a substantial step towards successful implementation of these methods. Despite some success so far in the field of tendon segmentation, demand still exists for a reliable method of segmentation that is robust to the confounding factors present in clinical ultrasound.

Texture analysis is a promising method for differentiation of the healing stages of a tendon. Consequently, correlation of texture parameters such as entropy to the mechanical properties of the tendon *in vivo* as a predictive model to aid in assessment of therapeutic strategy represents a critical goal for the future. The realization of this goal would be best accomplished by the coupling of an ultrasound image data set with a mechanical and histological analysis of the imaged tendon. Such a goal is possible with a porcine animal model that closely approximates the properties of human tendon.

Further work with local cEMD calculations do not seem to be critically dependent on selection of pixel separation and region count in each direction. Reducing the set of images derived for each input image would substantially reduce the computation time required for the most time intensive step of the script. Searching for regions of interest with local directionality consistency appears to be a viable option for future research to

continue pursuing. As a general solution to calculate local directionality, this method could potentially be used for any application interested in the separation of regions in an image based on local spatial patterning.

APPENDICES

APPENDIX A

REPRESENTATIVE IMAGES OBTAINED FROM THE PHILIPS IU-22 ULTRASOUND SYSTEM

Displayed in Appendix A are frames representative of several dicom sets obtained from the Philips IU-22 Ultrasound System. Frame number was selected *via* random number generator. The only processing performed on these images involved the removal of personal identifiers in the banner.

Figure A.1: Frame 132 of FLL93.

Figure A.2: Frame 227 of FLL157io.

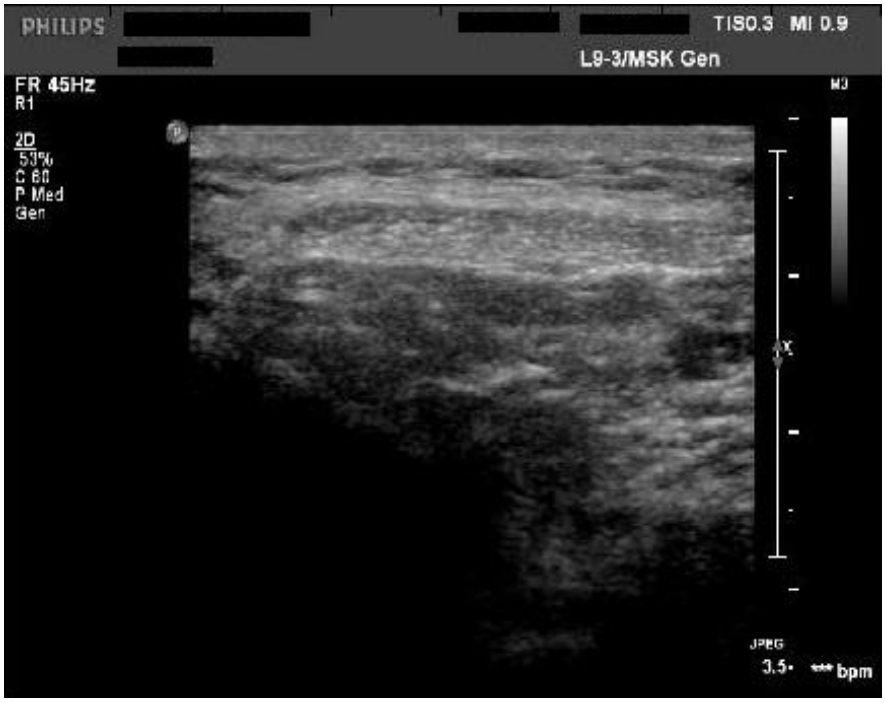

Figure A.3: Frame 217 of MTL93.

Figure A.4: Frame 522 of MLL93.

Figure A.5: Frame 638 of ML2L93.

APPENDIX B

SELECTED REGIONS OF INTEREST FOR ENTROPY CALCULATIONS AND USER-DEFINED MASK CIRCULAR EARTH MOVER'S DISTANCE COMPARATOR MATRIX

The images displayed below contain overlays in which a region was selected for a specific calculation. In the case of small tendinous region selection, the script iteration also selected the 16 by 16 mask for circular Earth Mover's Distance calculations to be centered on center pixel of the region selected for entropy analysis. The figures below are organized by dicom set; for each dicom set shown, four images are displayed, corresponding to the following images.

- Top left: Small Tendon Selection.
- Top Right: Small Background Selection.
- Bottom Left: Large Tendon Selection.
- Bottom Right: Large Background Selection.

The dicom sets chosen for display were selected by random number generation. FLL157io was removed from eligibility due to its extensive use in example calculations. The regions shown selected were used for all frames of the dicom set to which it belonged.

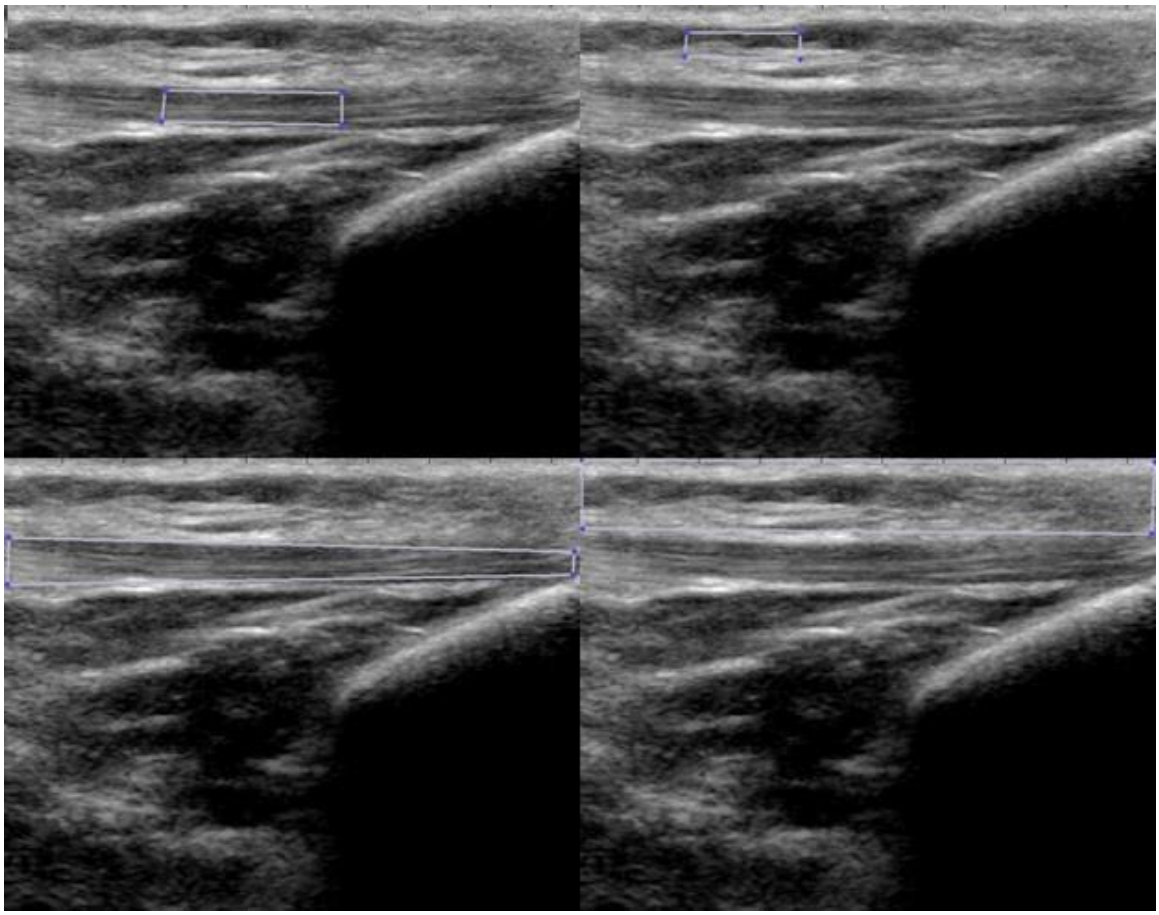

Figure B.1: Region Selections for FLL93.

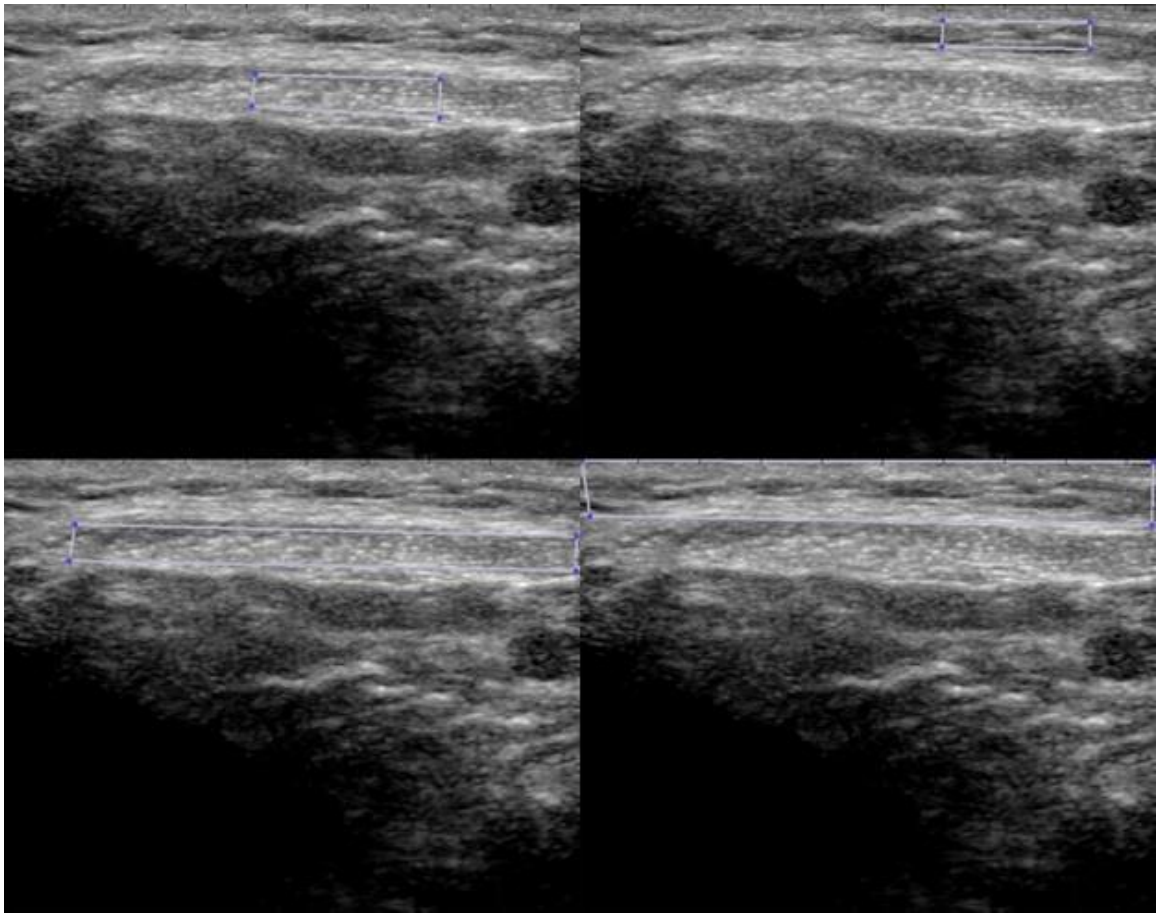

Figure B.2: Region Selections for MTL93.

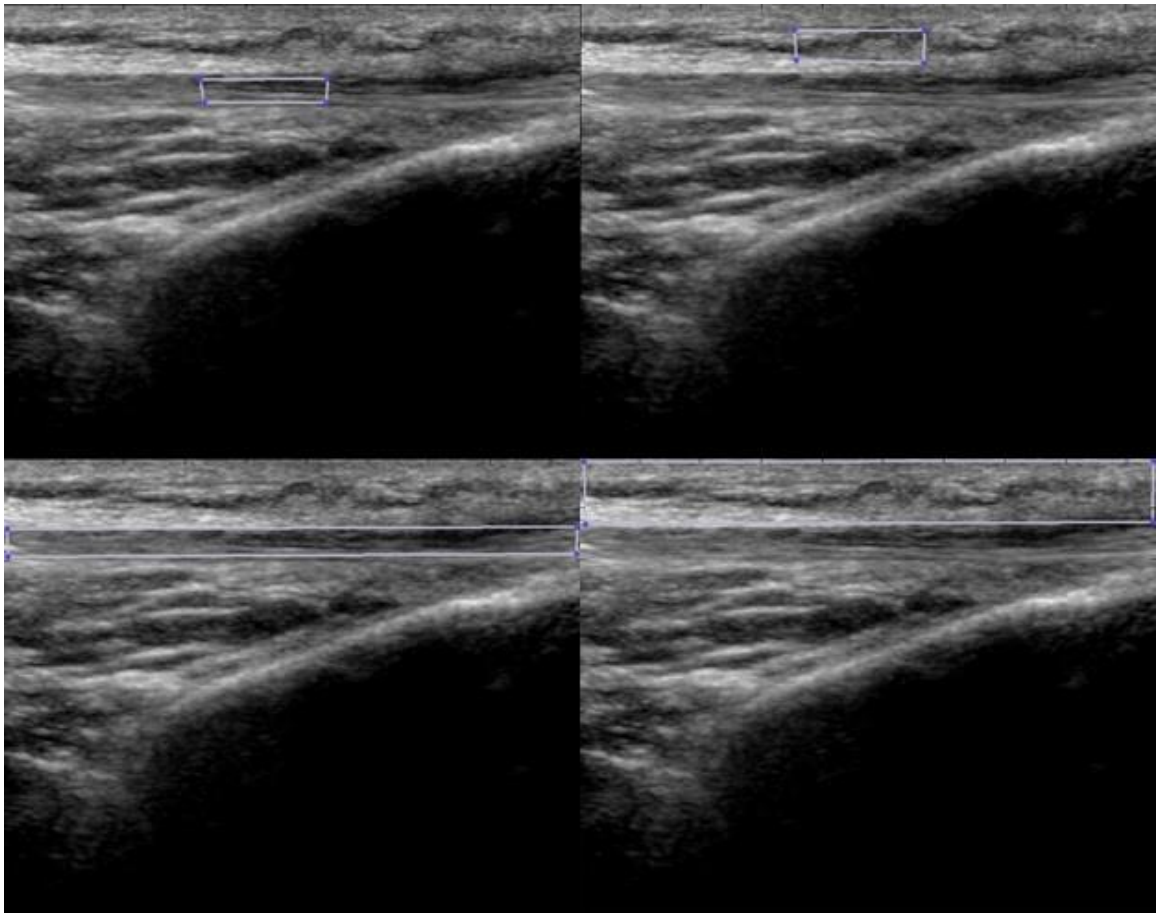

Figure B.3: Region Selections for ML2L93.

APPENDIX C

PARAMETERIZATION OF ULTRASOUND IMAGES: MEAN INTENSITY, DISCRETE LAPLACIAN, AND CIRCULAR EARTH MOVER'S DISTANCE

Each figure displayed below represents a randomly selected frame of a separately dicom set. Order of display for each figure will be as follows:

- Top left: Original image.
- Top right: Local Mean Intensity Image.
- Bottom left: Discrete Laplacian
- Bottom right: Circular Earth Mover's Distance

The circular Earth Mover's Distance depicted in Appendix C relates the local region's energy vector to the user-defined mask's energy vector. The dicom sets and frames shown below were selected by random number generation within each dicom set. FLL157io was excluded from eligibility due to its extensive use in example calculations.

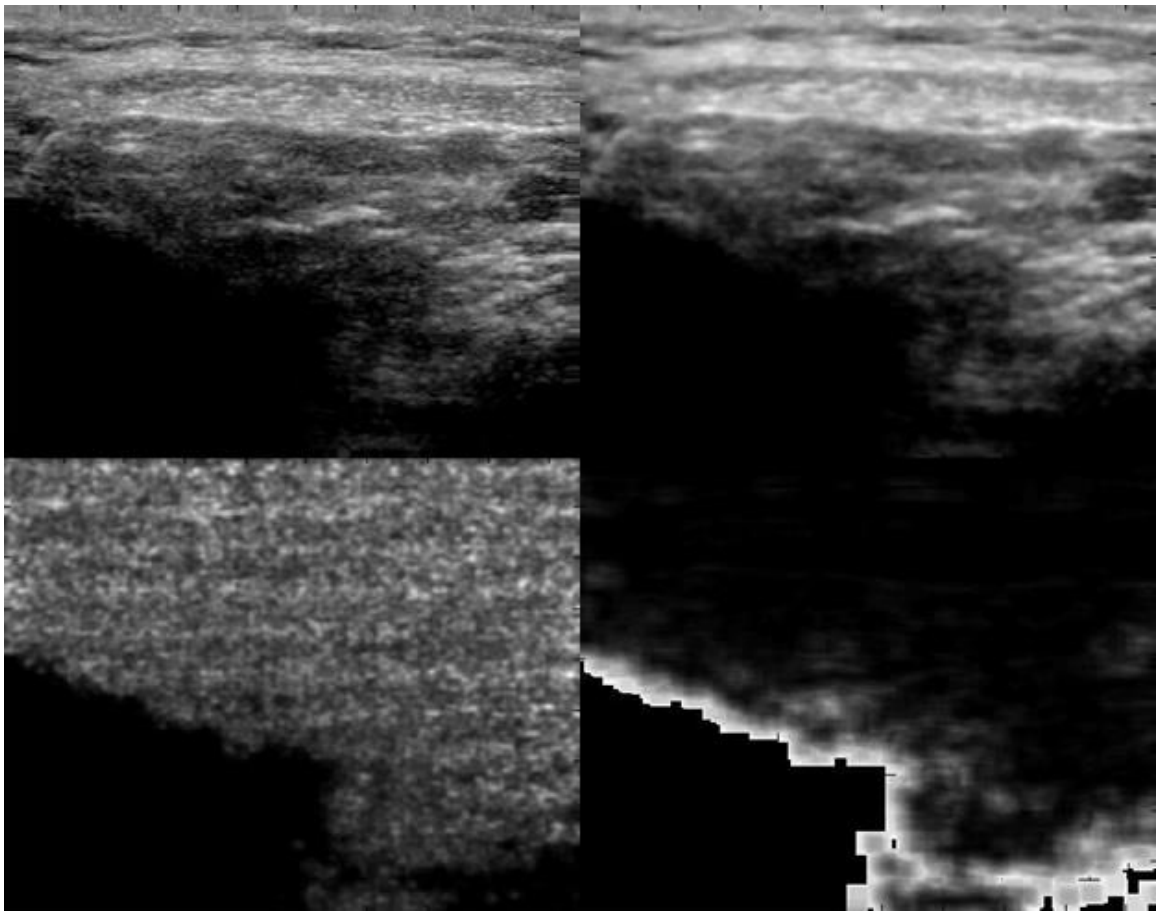

Figure C.1: Computed matrices for MTL93 Frame 16.

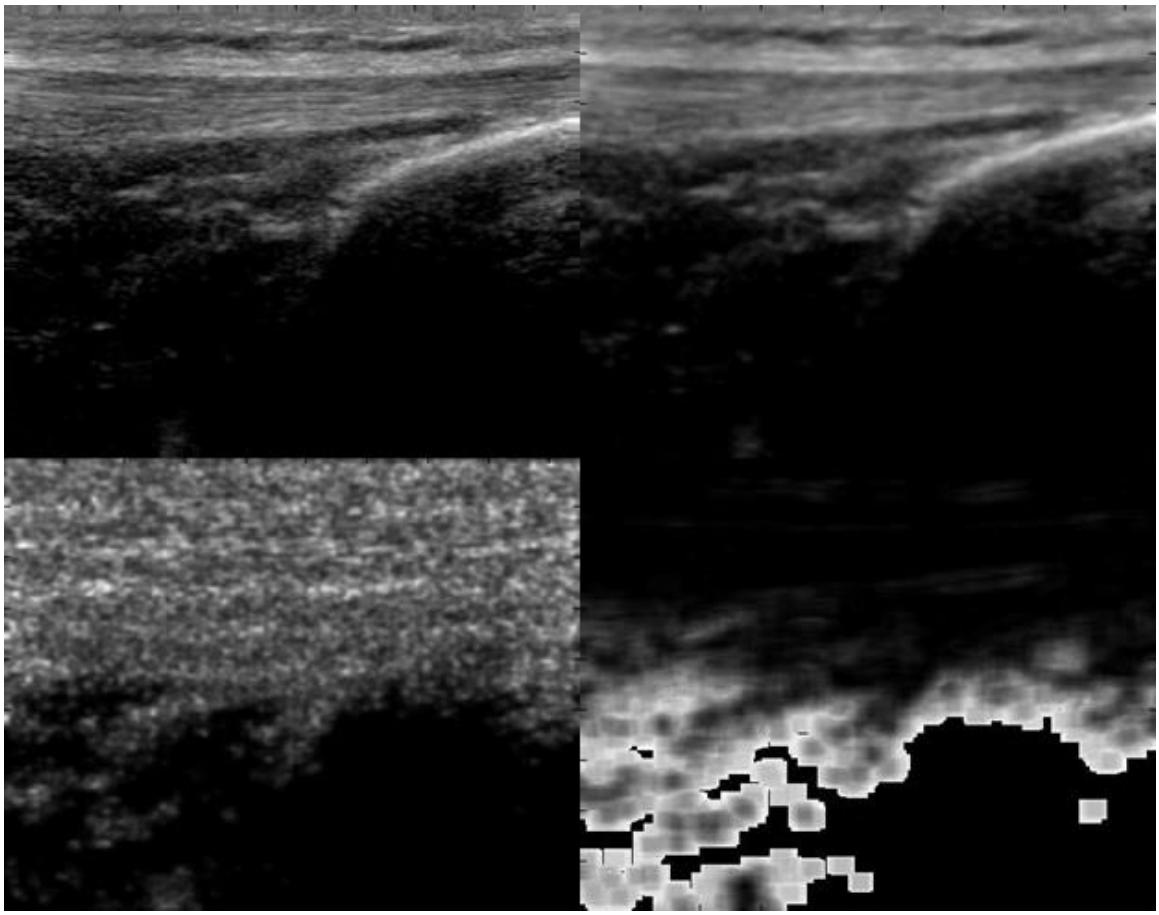

Figure C.2: Computed matrices for MLL93 Frame 36.

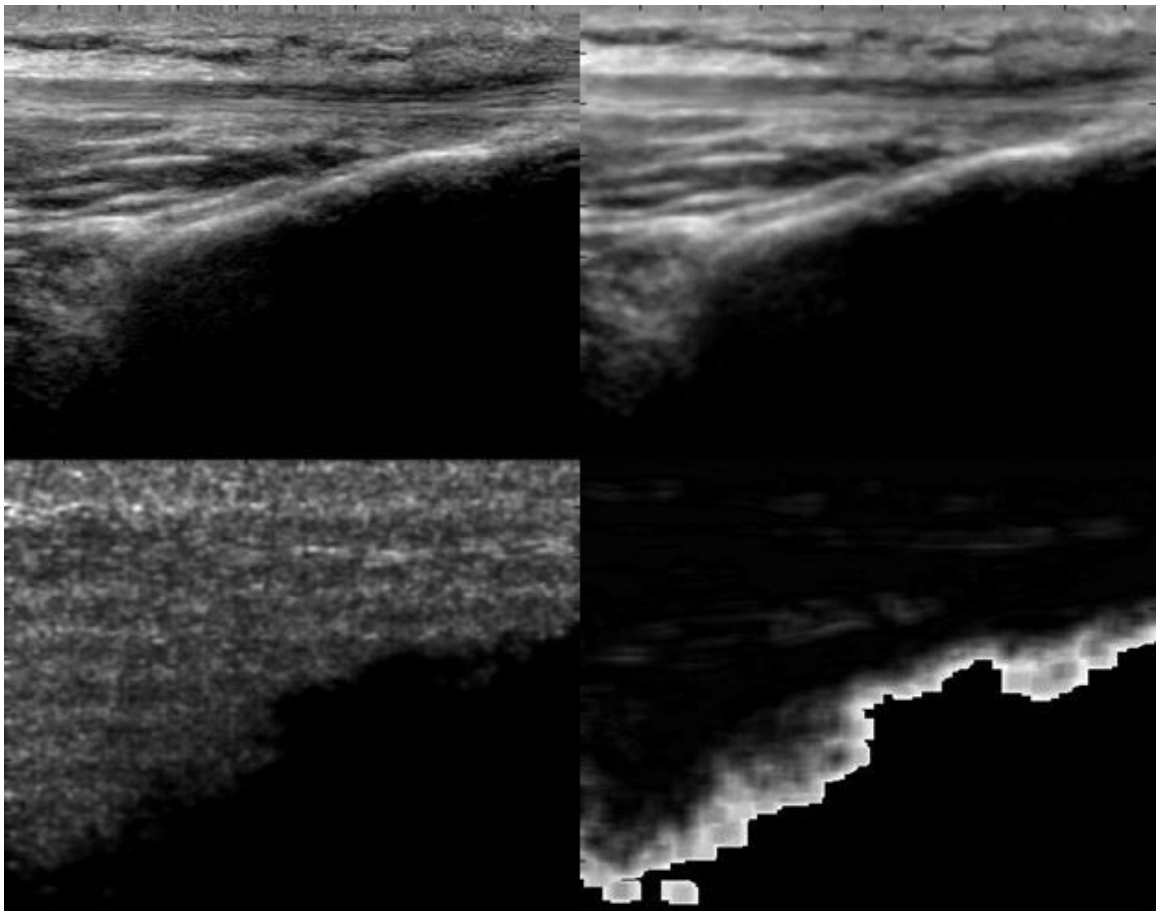

Figure C.3: Computed matrices for ML2L93 Frame 30.

APPENDIX D

STANDARD MEAN AND GAUSSIAN WEIGHTED AVERAGE CIRCULAR EARTH MOVER'S DISTANCE CALCULATIONS FOR LOCAL DIRECTIONAL CONSISTENCY

Standard mean and Gaussian weighted average calculations were computed as a metric of local directional consistency. For clarity, all matrices will be displayed after a base 10 logarithm operation is applied to offset the large numeric range present in most calculated cEMD matrices. Matrices for a random frame were chosen from each dicom set for which the second pass was computed is displayed below. For each figure, images will be displayed in the following order:

- Top left: Original Image
- Top right: User-defined mask-associated cEMD
- Row 2, left: One pixel separation, 16 regions in each direction standard mean
- Row 2, right: One pixel separation, 16 regions in each direction Gaussian weighted average
- Row 3, left: Four pixel separation, eight regions in each direction standard mean
- Row 3, right: Four pixel separation, eight regions in each direction Gaussian weighted average
- Row 4, left: Eight pixel separation, four regions in each direction standard mean
- Row 4, right: Eight pixel separation, four regions in each direction Gaussian weighted average
- Row 5, left: 16 pixel separation, two regions in each direction standard mean

- Row 5, right: 16 pixel separation, two regions in each direction Gaussian weighted average

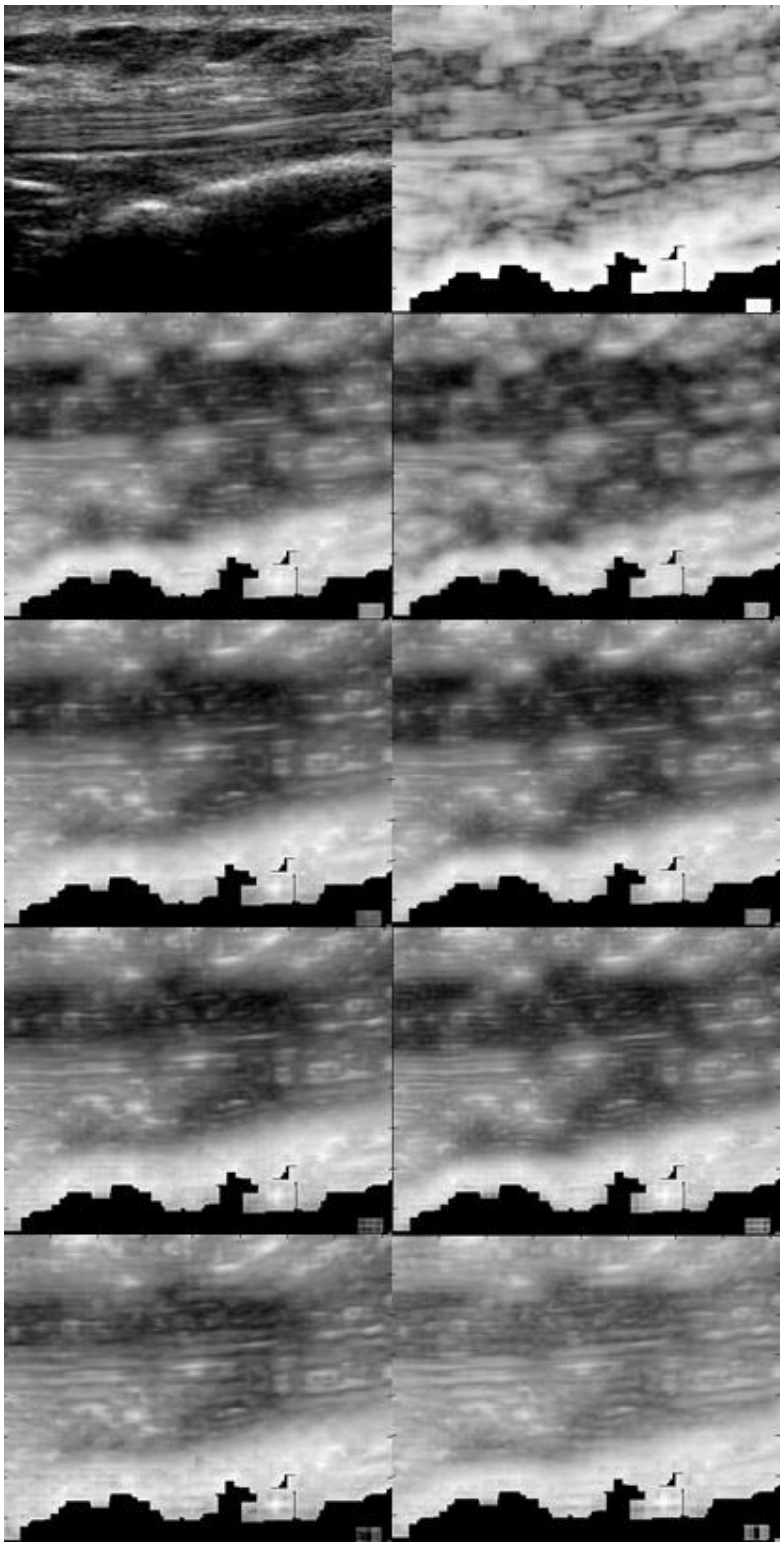

Figure D.1: cEMD calculations for FLL157io Frame 78.

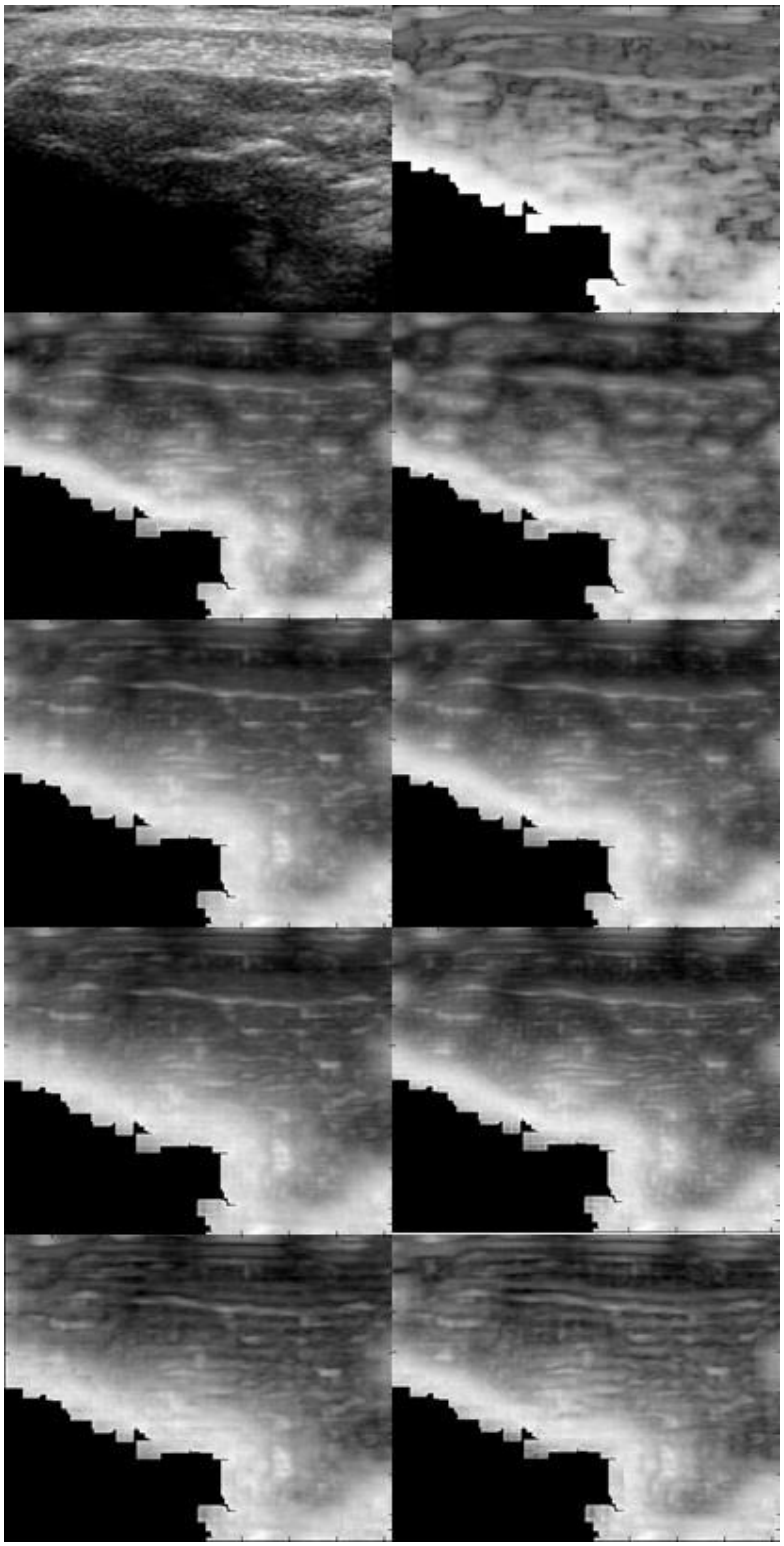

Figure D.2: cEMD calculations for MTL93 Frame 34.

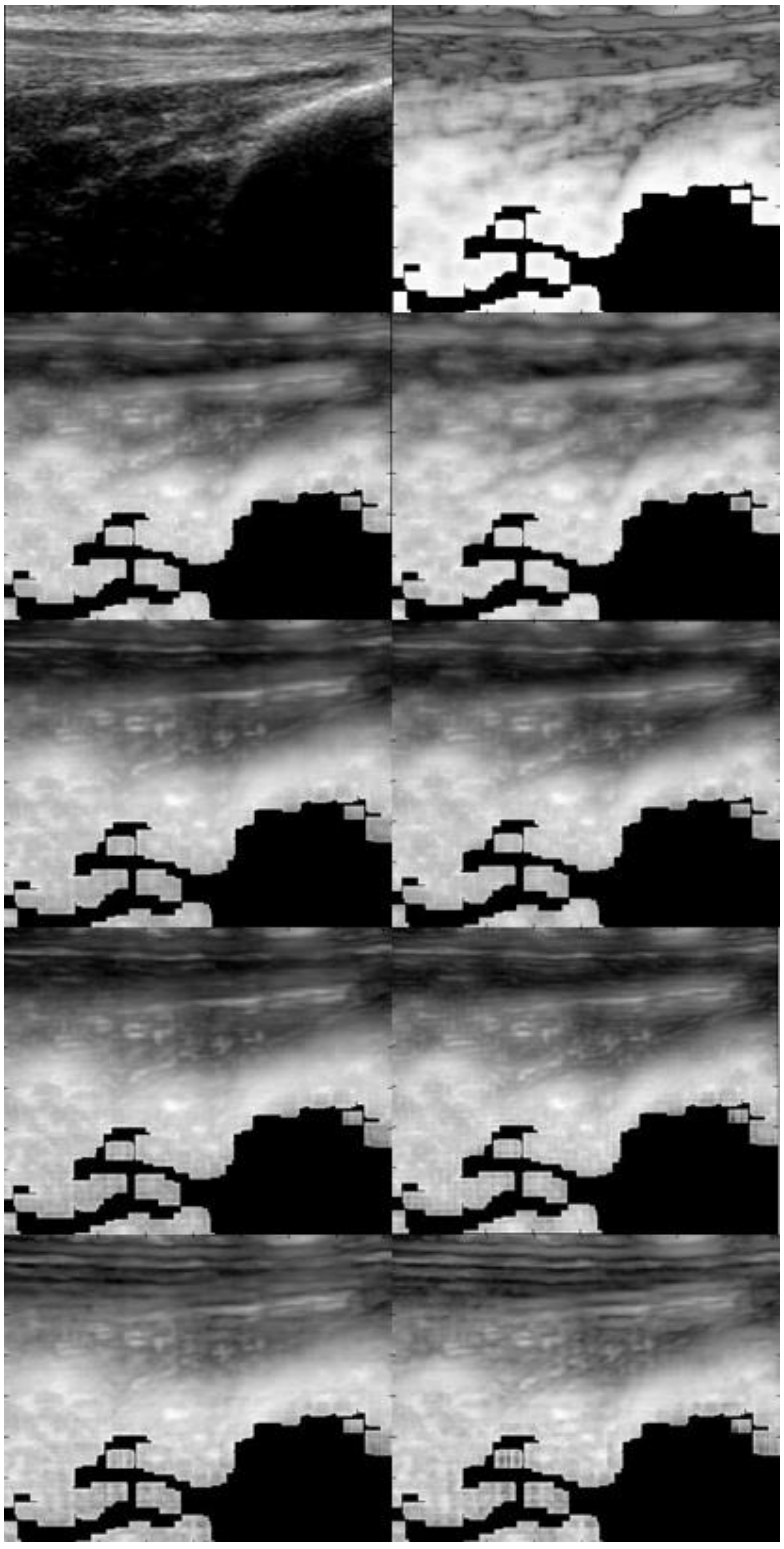

Figure D.3: cEMD calculations for MLL93 Frame 21.

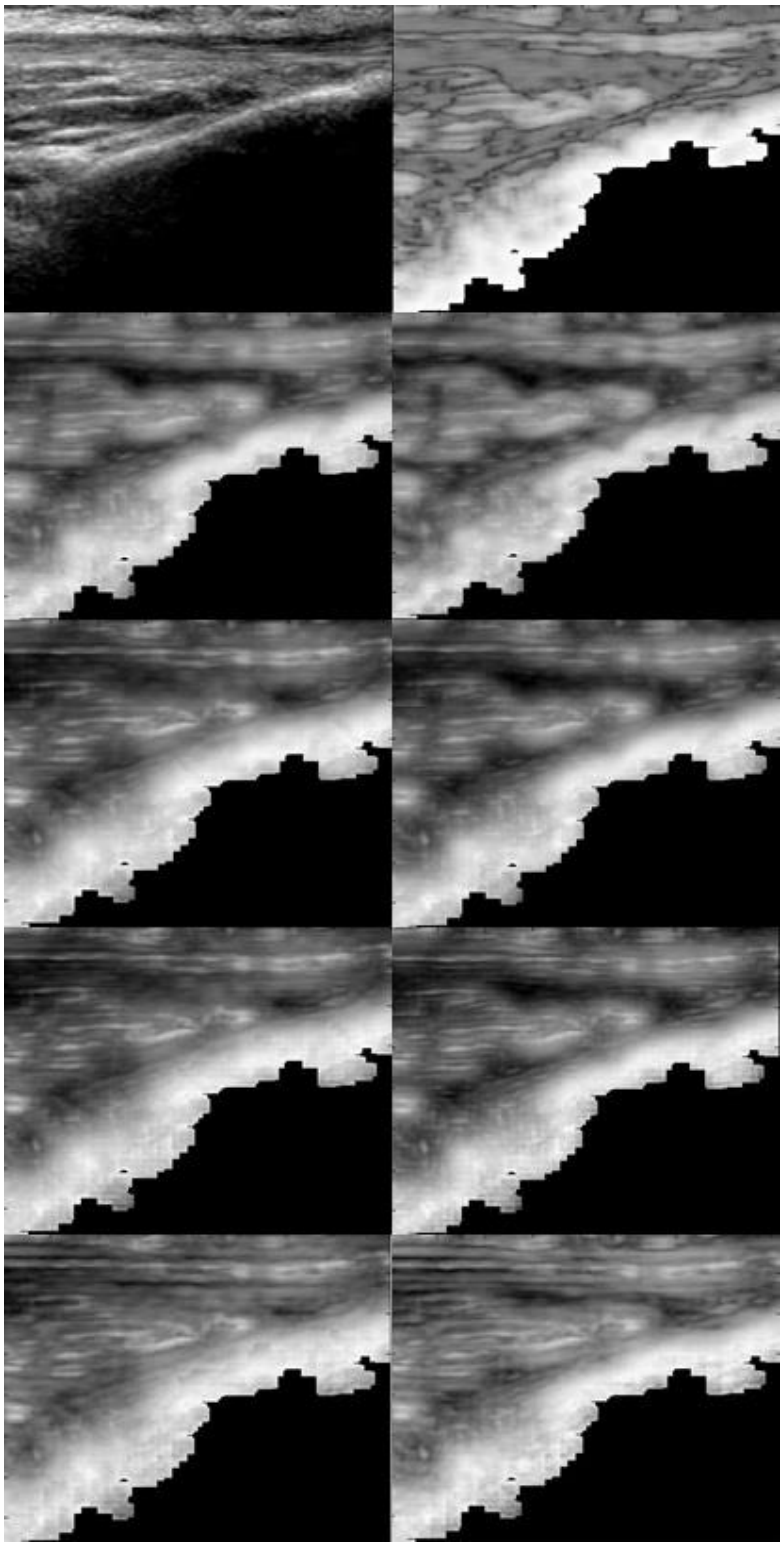

Figure D.4: cEMD calculations for ML2L93 Frame 33.

APPENDIX E

MATLAB SCRIPTS

Function TendonCalculations was the primary script used for texture analysis. Function trimmer was used remove empty borders from the output once the structure was completed, and used for display purposes and image registration. Transcriptions of both scripts are provided below.

```
function[stats, Contrast, Correlation, Energy, CoEntropy, PDFEntropy] =
TendonCalculations(dicomfile) %requires dicom string name for input

videoin = im2double(squeeze(mean(dicomread(dicomfile),3)));
numframes = size(videoin, 3);
sampdist= 1; %Change this value to manipulate the sampling distance
between frames

videoin = videoin(:,:,1:sampdist:numframes);
numframes = size(videoin, 3);

%Image Region without info border
i=dicominfo(dicomfile);
minx=i.SequenceOfUltrasoundRegions.Item_1.RegionLocationMinX0+125;
miny=i.SequenceOfUltrasoundRegions.Item_1.RegionLocationMinY0+35;
maxx=i.SequenceOfUltrasoundRegions.Item_1.RegionLocationMaxX1-125;
maxy=i.SequenceOfUltrasoundRegions.Item_1.RegionLocationMaxY1-35;

%Displays ultrasound image to user
imagein = videoin(miny:maxy,minx:maxx,1);
figure(1)
set(1,'Position', [10,10,1000,750])
colormap gray
imagesc(imagein);


%Prompts user for region of interest
[~,xi,yi] = roipoly;
close(1)
newimgin =
imagein(round(yi(1)):round(yi(3)),round(xi(1)):round(xi(3)));
maxi = max(max(newimgin));
normimgin = newimgin./maxi; %normalize input region to pdf
numpixels = sum(size(normimgin));
center = [round((size(normimgin,1))/2), round((size(normimgin,2))/2)];
mask = normimgin(center(1,1)-7:center(1,1)+8,center(1,2)-
7:center(1,2)+8);
clear imagein
```

```
%Begin texture analysis calculations
stats.frame(numframes) =
struct('Contrast',0,'Correlation',0,'Energy',0);
for frame = 1:numframes
    %First frame must initialize some variables
    if frame == 1

        comatrix = graycomatrix(normimgin, 'NumLevels', maxi);
%Calculate cooccurrence matrix

        %Stores some desired metrics in output structure
        stats.frame(1) = graycoprops(comatrix,
{'Contrast','Correlation', 'Energy'});
        stats.frame(1).Energy = (stats.frame(1).Energy)/numpixels;
        stats.frame(1).CoEntropy = 0;

        %Calculates entropy from the cooccurrence matrix
        comatrix(comatrix == 0) = eps;
        for x = 1:size(comatrix,1)
            for y = 1:size(comatrix,2)
                stats.frame(1).CoEntropy = stats.frame(1).CoEntropy +
(comatrix(x,y)*log2(comatrix(x,y)));
            end
        end
        stats.frame(1).CoEntropy =
(stats.frame(1).CoEntropy)/numpixels;



        %Calculates entropy from the probability density function
        [counts, ~] = imhist(normimgin, maxi);
        counts(counts == 0) = eps;
        counts = counts./sum(counts);
        stats.frame(1).PDFEntropy = (-
sum(counts.*log2(counts)))/numpixels;
        clear comatrix

    else  %Same function as first frame for all other frames
       imagein = videoin(miny:maxy,minx:maxx,frame);
       newimgin =
imagein(round(yi(1)):round(yi(3)),round(xi(1)):round(xi(3)));
       maxi = max(max(newimgin));
       normimgin = newimgin./maxi;
       comatrix = graycomatrix(normimgin, 'NumLevels', maxi);
       tempstats = graycoprops(comatrix, {'Contrast','Correlation',
'Energy'});
       stats.frame(1,frame).Contrast = tempstats.Contrast;
       stats.frame(1,frame).Correlation = tempstats.Correlation;
       stats.frame(1,frame).Energy = (tempstats.Energy)/numpixels;
       stats.frame(1,frame).CoEntropy=0;
       clear tempstats
```

```
        comatrix(comatrix == 0) = eps;
        for x = 1:size(comatrix,1)
             for y = 1:size(comatrix,2)
                 stats.frame(1,frame).CoEntropy =
stats.frame(1,frame).CoEntropy + (comatrix(x,y)*log2(comatrix(x,y)));
             end
        end
        stats.frame(1,frame).CoEntropy =
(stats.frame(1,frame).CoEntropy)/numpixels;

        [counts, ~] = imhist(normimgin, maxi);
        counts(counts == 0) = eps;
        counts = counts./sum(counts);
        stats.frame(frame).PDFEntropy = (-
sum(counts.*log2(counts)))/numpixels;

        clear comatrix
        clear imagein
    end
end

%Stores desired metrics into the output structure
for nframe = 1:numframes
    Contrast(nframe) = stats.frame(nframe).Contrast;
    Correlation(nframe) = stats.frame(nframe).Correlation;
    Energy(nframe) = stats.frame(nframe).Energy;
    CoEntropy(nframe) = stats.frame(nframe).CoEntropy;
    PDFEntropy(nframe) = stats.frame(nframe).PDFEntropy;
end



%End texture analysis, begin segmentation algorithm



%First pass begins here that initializes the data storing structure and
%begins analysis related to cEMD-mask
stats.fourier(numframes) =
struct('MaskEMDValues',[],'GaussianLocalEMDValues',[],'AverageLocalEMDV
alues',[],'MIValues',[],'STDValues',[],'AnalyzedUSImage',[],'Combined',
[],'IndicesOfMinimumEMD',[]);
maskft = abs(fftshift(fft2(mask))); %Fourier Transform of mask

%quadrant locator that overlays as a mask over each windows to
calculate
%energy summation vector
locator = zeros(16);
for c=1:16,
    if c<=8,
        locator(c:17-c,c)=1;
    else
```

```
        locator(17-c:c,c)=1;
    end;
end;
q1=locator(1:8,9:16);
q2=locator(1:8,1:8);
q3=locator(9:16,1:8);
q4=locator(9:16,9:16);

%Mask energy vector is calculated at 45 degree phase angles
for bin=1:8,
    maskenergy(bin)=0;
    for r=1:8,
       for c=1:8;
           if bin==1,
               if q1(r,c)==1,
                  maskenergy(bin)=maskenergy(bin)+(maskft(r,8+c))^2;
               end
           elseif bin==2,
               if q1(r,c)==0,
                  maskenergy(bin)=maskenergy(bin)+(maskft(r,8+c))^2;
               end
           elseif bin==3,
               if q2(r,c)==0,
                  maskenergy(bin)=maskenergy(bin)+(maskft(r,c))^2;
               end
           elseif bin==4,
               if q2(r,c)==1,
                  maskenergy(bin)=maskenergy(bin)+(maskft(r,c))^2;
               end
           elseif bin==5,
               if q3(r,c)==1,
                  maskenergy(bin)=maskenergy(bin)+(maskft(8+r,c))^2;
               end
           elseif bin==6,
               if q3(r,c)==0,
                  maskenergy(bin)=maskenergy(bin)+(maskft(8+r,c))^2;
               end
           elseif bin==7,
               if q4(r,c)==0,
                  maskenergy(bin)=maskenergy(bin)+(maskft(8+r,8+c))^2;
               end
           elseif bin==8,
               if q4(r,c)==1,
                  maskenergy(bin)=maskenergy(bin)+(maskft(8+r,8+c))^2;
               end
           end
       end
    end
end

%sanitizes input in the event of a 0 input mask
if sum(maskenergy)~=0,
    maskenergy=maskenergy./sum(maskenergy);
```

```
end

%Begin mask-compared cEMD calculations
indEMDmin=[1,1];
numbins = 8; %number of bins for 45 degree phase angle in circle
for ftframe=1:numframes
    imagein = padarray((videoin(miny:maxy,minx:maxx,ftframe)), [8,8],
'replicate','both');
    stats.fourier(ftframe).AnalyzedUSImage = imagein;
    [m,n] = size(imagein);
    blurmask = fspecial('gaussian',[15 15],2);
    mimap = imfilter(imagein,blurmask,'same');
    stdmap = imfilter(abs(del2(imagein)),blurmask,'same');
    mimap = mimap(8:m-8,8:n-8);
    stdmap = stdmap(8:m-8,8:n-8);
    stats.fourier(ftframe).MIValues = mimap;
    stats.fourier(ftframe).STDValues = stdmap;
    comb = mimap.*stdmap;
    minEMD=65535;
    sepmat = [1,4,8,16]; % define region of interest comparison
distance matrix
    numbox = [16,8,4,2]; % define number of regions of interest in each
direction to compare cEMD with the current region matrix
    for row=8:m-8, %per row raster
        loop=1;
        for col=8:n-8, %per column raster
            roi(row,col,:,:) = imagein(row-7:8+row,col-7:8+col);
%define 16x16 region of interest
            roift(row,col,:,:) =
abs(fftshift(fft2(squeeze(roi(row,col,:,:))))); %calculate the 2D
Fourier transform of the roi
            for bin=1:numbins, %8 bins created for 45 degree phase
angles of the 2D Fourier transform
                roienergy(row,col,bin)=0; %initialize energy total for
phase angles
                for r=1:8, %per row within the region of interest
                   for c=1:8; %per column within the region of interest
                       if bin==1,
                           if q1(r,c)==1,

roienergy(row,col,bin)=roienergy(row,col,bin)+(roift(row,col,r,8+c))^2;
                           end
                       elseif bin==2,
                           if q1(r,c)==0,

roienergy(row,col,bin)=roienergy(row,col,bin)+(roift(row,col,r,8+c))^2;
                           end
                       elseif bin==3,
                           if q2(r,c)==0,

roienergy(row,col,bin)=roienergy(row,col,bin)+(roift(row,col,r,c))^2;
                           end
                       elseif bin==4,
```

```
                            if q2(r,c)==1,

roienergy(row,col,bin)=roienergy(row,col,bin)+(roift(row,col,r,c))^2;
                            end
                        elseif bin==5,
                            if q3(r,c)==1,

roienergy(row,col,bin)=roienergy(row,col,bin)+(roift(row,col,8+r,c))^2;
                            end
                        elseif bin==6,
                            if q3(r,c)==0,

roienergy(row,col,bin)=roienergy(row,col,bin)+(roift(row,col,8+r,c))^2;
                            end
                        elseif bin==7,
                            if q4(r,c)==0,

roienergy(row,col,bin)=roienergy(row,col,bin)+(roift(row,col,8+r,8+c))^
2;
                            end
                        elseif bin==8,
                            if q4(r,c)==1,

roienergy(row,col,bin)=roienergy(row,col,bin)+(roift(row,col,8+r,8+c))^
2;
                            end
                        end
                    end
                end
            end
            if sum(roienergy(row,col,:))~=0,

roienergy(row,col,:)=roienergy(row,col,:)./sum(roienergy(row,col,:));
%normalize mass in each transform's energy total
            end
            roienergymaskmat = roienergy;
            EMD=[];
            for EMDbin=1:numbins,
                diff = roienergymaskmat(row,col,EMDbin)-
maskenergy(EMDbin);
                if sum(roienergymaskmat(row,col,:))~=0,
                    if EMDbin~=8,

roienergymaskmat(row,col,EMDbin+1)=roienergymaskmat(row,col,EMDbin+1)+d
iff;

roienergymaskmat(row,col,EMDbin)=roienergymaskmat(row,col,EMDbin)-diff;
                        EMD(EMDbin)=diff;
                    else
                        EMD(EMDbin)=0;
                    end
                else
                    EMD(EMDbin)=10000;
                end
```

```
            end
            if sum(abs(EMD-median(EMD))) < 80000,
                cEMDsum = sum(abs(EMD-median(EMD)));
            else
                cEMDsum = 255;
            end
            stats.fourier(ftframe).MaskEMDValues(row-7,col-7) =
cEMDsum;
            diff=[];
            if cEMDsum<minEMD && cEMDsum~=0,
                minEMD=cEMDsum;
                indEMDmin=[row-7,col-7];
            end
        end
    end
    %End mask-related cEMD calculations


    %Begin local region cEMD calculations
    for i=8:m-8, %second pass used for local region cEMD calculations
        loop=2;
        for j=8:n-8, %column raster for local region cEMD calculations
            if i>=41&&i<=m-41, % bulk row test
                if j>=41&&j<=n-41, %bulk column test
                    for boxnumtype=1:4,
                        % seppixels=1,4,8,16; numboxes=16,8,4,2;
                        seppixels=sepmat(1,boxnumtype);
                        numboxes=numbox(1,boxnumtype);
                        for boxcomp=1:numboxes,
                            roiendir(1,boxcomp,:)=squeeze(roienergy(i-
(seppixels*boxcomp),j-(seppixels*boxcomp),:));
                            roiendir(2,boxcomp,:)=squeeze(roienergy(i-
(seppixels*boxcomp),j,:));
                            roiendir(3,boxcomp,:)=squeeze(roienergy(i-
(seppixels*boxcomp),j+(seppixels*boxcomp),:));

roiendir(4,boxcomp,:)=squeeze(roienergy(i,j-(seppixels*boxcomp),:));

roiendir(5,boxcomp,:)=squeeze(roienergy(i,j+(seppixels*boxcomp),:));

roiendir(6,boxcomp,:)=squeeze(roienergy(i+(seppixels*boxcomp),j-
(seppixels*boxcomp),:));

roiendir(7,boxcomp,:)=squeeze(roienergy(i+(seppixels*boxcomp),j,:));

roiendir(8,boxcomp,:)=squeeze(roienergy(i+(seppixels*boxcomp),j+(seppix
els*boxcomp),:));
                            for dir=1:8,
                                intercEMD=[];
                                roiencurrent=squeeze(roienergy(i,j,:));
                                for bins=1:numbins,
                                    diff=roiencurrent(bins)-
roiendir(dir,boxcomp,bins);
```

```
                                    if
sum(roiencurrent~=0)&&sum(roiendir(dir,boxcomp,:))~=0,
                                        if bins~=8,

roiencurrent(bins+1)=roiencurrent(bins+1)+diff;

roiencurrent(bins)=roiencurrent(bins)-diff;
                                            intercEMD(bins)=diff;
                                        else
                                            intercEMD(bins)=0;
                                        end
                                    else
                                        intercEMD(bins)=10000;
                                    end
                                end
                                if sum(abs(intercEMD-
median(intercEMD))) < 80000,
                                    intercEMDsum = sum(abs(intercEMD-
median(intercEMD)));
                                else
                                    intercEMDsum = 255;
                                end
                                groupcEMD(dir,boxcomp)=intercEMDsum;
                            end
                        end


                        % Calculates Gaussian weighting vector to apply
                        % outward from the center of the region
                        gblur=gausswin(2*numboxes)';

gblur=repmat(gblur(1,(numboxes+1):(2*numboxes)),8,1);

gaussmap(boxnumtype,i,j)=mean(mean(gblur.*groupcEMD));
                        avgmap(boxnumtype,i,j)=mean(mean(groupcEMD));
                        groupcEMD=[];
                    end

                    %Stores calculated cEMD values in the relevant
                    %structure
                    for type=1:4,
                        if type==1,

stats.fourier(ftframe).GaussianLocalEMDValues.sep1box16(i,j) =
gaussmap(type,i,j);

stats.fourier(ftframe).AverageLocalEMDValues.sep1box16(i,j) =
avgmap(type,i,j);
                        elseif type==2,

stats.fourier(ftframe).GaussianLocalEMDValues.sep4box8(i,j) =
gaussmap(type,i,j);
```

```
stats.fourier(ftframe).AverageLocalEMDValues.sep4box8(i,j) =
avgmap(type,i,j);
                        elseif type==3,

stats.fourier(ftframe).GaussianLocalEMDValues.sep8box4(i,j) =
gaussmap(type,i,j);

stats.fourier(ftframe).AverageLocalEMDValues.sep8box4(i,j) =
avgmap(type,i,j);
                        elseif type==4.

stats.fourier(ftframe).GaussianLocalEMDValues.sep16box2(i,j) =
gaussmap(type,i,j);

stats.fourier(ftframe).AverageLocalEMDValues.sep16box2(i,j) =
avgmap(type,i,j);
                        end
                    end
                end
            end
        end
    end
    stats.fourier(ftframe).IndicesOfMinimumEMD = indEMDmin;
    stats.fourier(ftframe).Combined = comb;
end
```

Begin function trimmer

```
function [outmat,regmat] = trimmer(inmat)
    eval([inmat,'c']) = inmat;
    numframes = 134;   %Change this value to the number of frames in
the input
    for i =1:numframes,
        eval([inmat,'c']).fourier(i).AnalyzedUSImage =
eval([inmat,'c']).fourier(i).AnalyzedUSImage(8:455,8:482);
        eval([inmat,'c']).fourier(i).AnalyzedUSImage =
eval([inmat,'c']).fourier(i).AnalyzedUSImage(33:(448-34),33:(475-34));
        eval([inmat,'c']).fourier(i).MaskEMDValues =
eval([inmat,'c']).fourier(i).MaskEMDValues(33:(448-34),33:(475-34));
        eval([inmat,'c']).fourier(i).MIValues =
eval([inmat,'c']).fourier(i).MIValues(33:(448-34),33:(475-34));
        eval([inmat,'c']).fourier(i).STDValues =
eval([inmat,'c']).fourier(i).STDValues(33:(448-34),33:(475-34));
        eval([inmat,'c']).fourier(i).Combined =
eval([inmat,'c']).fourier(i).Combined(33:(448-34),33:(475-34));
        eval([inmat,'c']).fourier(i).GaussianLocalEMDValues.sep4box8 =
eval([inmat,'c']).fourier(i).GaussianLocalEMDValues.sep4box8(41:422,41:
449);
        eval([inmat,'c']).fourier(i).AverageLocalEMDValues.sep4box8 =
eval([inmat,'c']).fourier(i).AverageLocalEMDValues.sep4box8(41:422,41:4
49);
```

```
        eval([inmat,'c']).fourier(i).GaussianLocalEMDValues.sep1box16 =
eval([inmat,'c']).fourier(i).GaussianLocalEMDValues.sep1box16(41:422,41
:449);
        eval([inmat,'c']).fourier(i).GaussianLocalEMDValues.sep8box4 =
eval([inmat,'c']).fourier(i).GaussianLocalEMDValues.sep8box4(41:422,41:
449);
        eval([inmat,'c']).fourier(i).GaussianLocalEMDValues.sep16box2 =
eval([inmat,'c']).fourier(i).GaussianLocalEMDValues.sep16box2(41:422,41
:449);
        eval([inmat,'c']).fourier(i).AverageLocalEMDValues.sep1box16 =
eval([inmat,'c']).fourier(i).AverageLocalEMDValues.sep1box16(41:422,41:
449);
        eval([inmat,'c']).fourier(i).AverageLocalEMDValues.sep8box4 =
eval([inmat,'c']).fourier(i).AverageLocalEMDValues.sep8box4(41:422,41:4
49);
        eval([inmat,'c']).fourier(i).AverageLocalEMDValues.sep16box2 =
eval([inmat,'c']).fourier(i).AverageLocalEMDValues.sep16box2(41:422,41:
449);
    end

    %Below this line relates to image display for a frame of interest
and
    %image registration
    F1US = eval([inmat,'c']).fourier(1).AnalyzedUSImage;
    F1Comb = eval([inmat,'c']).fourier(1).Combined;
    F1STD = eval([inmat,'c']).fourier(1).STDValues;
    F1CGS4B8 =
eval([inmat,'c']).fourier(1).Combined.*eval([inmat,'c']).fourier(1).Gau
ssianLocalEMDValues.sep4box8;
    F1GS4B8 =
eval([inmat,'c']).fourier(1).GaussianLocalEMDValues.sep4box8;
    GS4B8F1F2avg =
eval([inmat,'c']).fourier(1).GaussianLocalEMDValues.sep4box8.*eval([inm
at,'c']).fourier(2).GaussianLocalEMDValues.sep4box8;

    figure(1); colormap gray; imagesc(F1US); %ultrasound image
    figure(2); colormap gray; imagesc(F1Comb); %combined mi/std image
    figure(3); colormap gray; imagesc(F1GS4B8); %gaussian emd first
frame
    figure(4); colormap gray; imagesc(F1CGS4B8); %comb.*gaussian
    figure(5); colormap gray; imagesc(log10(F1GS4B8)); %log10 gaussian
    figure(6); colormap gray; imagesc(log10(GS4B8F1F2avg)); %2 frame
avg gaussian log 10

    %image registration process
    [optimizer,metric] = imregconfig('multimodal');
    for x=1:numframes,
        RegMat(:,:,x) =
eval([inmat,'c']).fourier(x).GaussianLocalEMDValues.sep4box8;
    end
    regGS4B8avg = RegMat(:,:,1);
    for y=2:numframes,
        fixed = RegMat(:,:,y-1);
```

```
        moving = RegMat(:,:,y);
        movingReg =
imregister(moving,fixed,'translation',optimizer,metric);
        regGS4B8avg = regGS4B8avg.*movingReg;
        RegMat(:,:,y) = movingReg;
    end
    GS4B8avg =
eval([inmat,'c']).fourier(1).GaussianLocalEMDValues.sep4box8;
    for j = 2:numframes,
        GS4B8avg =
eval([inmat,'c']).fourier(j).GaussianLocalEMDValues.sep4box8.*GS4B8avg;
    end
    %end image registration process


    %display figures and store outputs
    figure(7); colormap gray; imagesc(log10(GS4B8avg)); %log10 total
gaussian avg no correction
    figure(8); colormap gray; imagesc(log10(regGS4B8avg)); %log10 total
gaussian avg with correction
    outmat = eval([inmat,'c']);
    regmat = RegMat;
end
```